

CO line emission from galaxies in the Epoch of Reionization

L. Vallini,¹★ A. Pallottini,^{2,3,4,5} A. Ferrara,^{3,6} S. Gallerani,³ E. Sobacchi^{7,8}
and C. Behrens³

¹Nordita, KTH Royal Institute of Technology and Stockholm University, Roslagstullsbacken 23, SE-10691 Stockholm, Sweden

²Centro Fermi, Museo Storico della Fisica e Centro Studi e Ricerche ‘Enrico Fermi’, Piazza del Viminale 1, Roma I-00184, Italy

³Scuola Normale Superiore, Piazza dei Cavalieri 7, I-56126 Pisa, Italy

⁴Kavli Institute for Cosmology, University of Cambridge, Madingley Road, Cambridge CB3 0HA, UK

⁵Cavendish Laboratory, University of Cambridge, 19 J. J. Thomson Ave., Cambridge CB3 0HE, UK

⁶Kavli IPMU, WPI, The University of Tokyo, Kashiwa, Chiba 277-8583, Japan

⁷Physics Department, Ben-Gurion University, P.O.B. 653, Beer-Sheva 84105, Israel

⁸Department of Natural Sciences, The Open University of Israel, 1 University Road, P.O.B. 808, Raanana 4353701, Israel

Accepted 2017 September 9. Received 2017 September 9; in original form 2017 June 29

ABSTRACT

We study the CO line luminosity (L_{CO}), the shape of the CO spectral line energy distribution (SLED), and the value of the CO-to- H_2 conversion factor in galaxies in the Epoch of Reionization (EoR). For this aim, we construct a model that simultaneously takes into account the radiative transfer and the clumpy structure of giant molecular clouds (GMCs) where the CO lines are excited. We then use it to post-process state-of-the-art zoomed, high resolution (30 pc), cosmological simulation of a main-sequence ($M_* \approx 10^{10} M_\odot$, $\text{SFR} \approx 100 M_\odot \text{ yr}^{-1}$) galaxy, ‘Althæa’, at $z \approx 6$. We find that the CO emission traces the inner molecular disc ($r \approx 0.5$ kpc) of Althæa with the peak of the CO surface brightness co-located with that of the [C II] 158 μm emission. Its $L_{\text{CO}(1-0)} = 10^{4.85} L_\odot$ is comparable to that observed in local galaxies with similar stellar mass. The high ($\Sigma_{\text{gas}} \approx 220 M_\odot \text{ pc}^{-2}$) gas surface density in Althæa, its large Mach number ($\mathcal{M} \approx 30$) and the warm kinetic temperature ($T_k \approx 45 \text{ K}$) of GMCs yield a CO SLED peaked at the CO(7–6) transition, i.e. at relatively high- J and a CO-to- H_2 conversion factor $\alpha_{\text{CO}} \approx 1.5 M_\odot (\text{K km s}^{-1} \text{ pc}^2)^{-1}$ lower than that of the Milky Way. The Atacama Large Millimeter/submillimeter Array observing time required to detect (resolve) at 5σ the CO(7–6) line from galaxies similar to Althæa is $\approx 13 \text{ h}$ ($\approx 38 \text{ h}$).

Key words: ISM: clouds – ISM: molecules – galaxies: high-redshift – galaxies: ISM – infrared: ISM.

1 INTRODUCTION

Constraining the properties of the molecular gas in galaxies at the end ($z \approx 6$) of the Epoch of Reionization (EoR) is a compelling step to understand the process of star formation in the first galaxies.

Molecular hydrogen (H_2), the most abundant molecule in the Universe, lacks of a permanent dipole moment and its first quadrupole line has an excitation temperature ($T_{\text{ex}} \approx 500 \text{ K}$) significantly higher than the kinetic temperatures ($T_k \approx 10\text{--}20 \text{ K}$) of giant molecular clouds (GMCs; McKee & Ostriker 2007). This is the reason why molecular gas in galaxies is very often traced through the detection of the rotational transitions the carbon monoxide, CO, the second most abundant molecule after H_2 . The first CO rotational transition is in fact characterized by $T_{\text{ex}} \approx 5 \text{ K}$, with critical density

$n_{\text{cr}} \approx 10^3 \text{ cm}^{-3}$ (Solomon & Vanden Bout 2005; Carilli & Walter 2013), i.e. it is easily excited within GMCs.

Noticeably, the different excitation requirements of the various CO lines ($T_{\text{ex}} \approx 5\text{--}300 \text{ K}$, $n_{\text{cr}} \approx 10^3\text{--}10^6 \text{ cm}^{-3}$ for upper state rotational quantum number $J_{\text{up}} = 1\text{--}10$) can be exploited to constrain gas properties (e.g. density, temperature) and the gas heating mechanisms (e.g. FUV photons, X-ray photons, cosmic rays, shocks). This can be done through the analysis of the so-called CO spectral line energy distribution (CO SLED)-flux in each emission line as a function of J_{up} (Kaufman et al. 1999; Meijerink, Spaans & Israel 2007; Obreschkow et al. 2009; Mashian et al. 2015; Rosenberg et al. 2015; Indriolo et al. 2017; Lu et al. 2017).

Searches for CO line emission at redshift $z > 5$ have been mainly focused on the most luminous sources like quasars (e.g. Bertoldi et al. 2003; Maiolino et al. 2007; Wang et al. 2010; Walter et al. 2012; Combes et al. 2012; Venemans et al. 2012; Gallerani et al. 2014, 2017, for a recent review) or powerful sub-millimeter galaxies (e.g. Riechers et al. 2010a; Weiß et al. 2013; Aravena

* E-mail: livia.vallini@su.se

et al. 2016). On the contrary, little is known regarding the molecular gas content of high- z normal star-forming galaxies – e.g. Lyman alpha emitters (LAEs) and/or Lyman break galaxies (LBGs) – which are more representative of the bulk of galaxy population at the end of EoR (e.g. Dayal, Ferrara & Gallerani 2008; Dayal et al. 2009; Vallini, Dayal & Ferrara 2012). Only a handful of CO detections have been reported in (mostly lensed) LBGs at $z \approx 3$ (Baker et al. 2004; Coppin et al. 2007; Riechers et al. 2010b; Livermore et al. 2012; Saintonge et al. 2013; Dessauges-Zavadsky et al. 2015, 2016; Ginolfi et al. 2017), while searches for low- J CO rotational lines in LAEs at $z \approx 6$ have resulted in non-detections (Wagg, Kanekar & Carilli 2009; Wagg & Kanekar 2012).

The Atacama Large Millimeter/submillimeter Array (ALMA) advent has opened new perspectives for the detection of CO rotational transitions from the EoR. It is more sensitive than the other submillimeter/millimeter facilities adopted in previous studies targeting LAEs/LBGs in the EoR and, more importantly, its receiver bands allow one to trace transitions with $J_{\text{up}} \geq 6$ (high- J , hereafter), from $z \geq 6$. This represents a key-point because the peak of the CO SLED in galaxies with high specific star formation rate (sSFR) is often associated with high- J transitions (Mashian et al. 2015), and such galaxies are common at high- z (Jiang et al. 2016). Those transitions, being more luminous than low- J ones, may represent a viable option to target molecular gas at the end of EoR.

The advent of ALMA has also triggered the development of – mostly semi-analytical – works that aim at modelling the CO emission signal from high-redshift ($z > 6$) galaxies (e.g. Obreschkow et al. 2009; Lagos et al. 2012; Vallini et al. 2012; da Cunha et al. 2013; Muñoz & Furlanetto 2013; Popping et al. 2016).

Obreschkow et al. (2009); Lagos et al. (2012) and Popping et al. (2016) combined semi-analytical galaxy formation simulations with sub-grid models devised to convert the molecular mass into CO luminosities, and predict the high- z evolution of the CO luminosity function (e.g. Walter et al. 2014; Decarli et al. 2016; Vallini et al. 2016). Those models account for e.g. the heating by the cosmic microwave background (CMB) (see also da Cunha et al. 2013), the Far-Ultraviolet (FUV) flux from starburst and/or by X-rays produced by active galactic nuclei. Vallini et al. (2012) used the semi-analytical model for the molecular fraction by Krumholz, McKee & Tumlinson (2009) to infer the CO luminosity from a sample of $z \approx 6$ LAEs extracted from cosmological simulations. However, the work by Obreschkow et al. (2009); Lagos et al. (2012); Vallini et al. (2012) lacked of a detailed description of the internal structure of GMCs. Muñoz & Furlanetto (2013) made a step forward in this direction. Using an analytical model, they explored the link between the GMC properties set by the turbulence and the physics of CO emission in high- z LBGs; they conclude that the CO signal could be very difficult to observe from $z > 6$. While Muñoz & Furlanetto (2013) catch some of the fundamental aspects of the internal structure and of the radiative transfer within the GMCs, this was at the expense of a full description of the galaxy formation process.

The goal of this work is to assess the feasibility of detecting CO lines from typical LBGs at high- z by simultaneously capturing the full cosmological context of high-redshift galaxy formation and the radiative transfer from the outer photodissociation regions (PDRs) (Hollenbach & Tielens 1999) up to the fully molecular inner part of GMCs. For this aim, we construct a physically motivated model that simultaneously takes into account the radiative transfer and the clumpy structure of GMCs. We then use it to post-process state-of-the-art zoomed cosmological simulations (Pallottini et al. 2017a,b). This type of a sub-grid approach has been already shown to be an

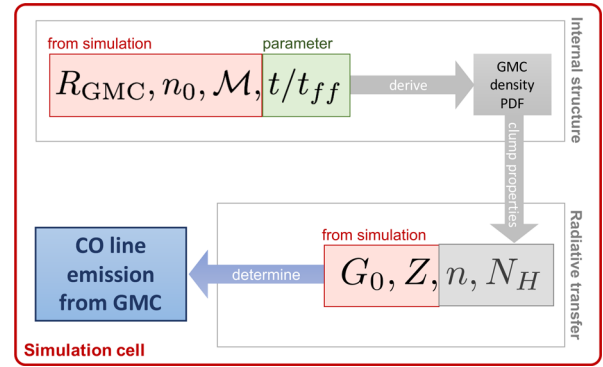


Figure 1. Outline of the model presented in this paper. The modelling of the GMC structure as a function of the cloud radius (R_{GMC}), mean number density (n_0), sonic Mach number (\mathcal{M}), and time (t/t_{ff}) is described in details in Section 2.1. The radiative transfer, as a function of FUV flux in Habing units (G_0), metallicity (Z), gas density (n) and column density (N_{H}) is discussed Section 2.2. The application of the sub-grid model to simulations is presented in Section 4.1.

optimal strategy to obtain predictions and insights on the luminosity of, e.g. [C II] 157.7 μm line emission tracing the neutral diffuse gas and dense PDRs (Vallini et al. 2013, 2015; Pallottini et al. 2015) in galaxies at the end or EoR. It allows one, on the one hand, to properly treat the small physical scales ($\approx 0.1 - 1$ pc) of clumps in GMCs, and the complex network of chemical and physical reactions in the PDR layer and in the fully molecular parts of GMCs. On the other hand, it benefits from the high-resolution hydrodynamical simulations by obtaining a proper description, down to scales of ≈ 30 pc, of the interstellar medium (ISM) density, turbulence level, metal enrichment and radiation field into which GMCs are embedded.

The paper is structured as follows. In Section 2 we describe how we implement the CO line emission calculation taking into account the internal density structure of GMCs. In Section 3 we validate the model against local observations. Finally, in Section 4, we apply the model to high-resolution cosmological simulations to compute the CO emission from normal star-forming galaxies at the end of EoR. We draw our conclusions in Section 5.

2 MODEL OUTLINE

The model strategy adopted in this work is summarized in Fig. 1, where we outline its modular structure. The first part (see Section 2.1) deals with the analytical description of the *internal density structure* of GMCs and its time evolution. The second part concerns the *radiative transfer* performed to compute the CO line emission once the density field is established (see Section 2.2). The sub-grid model is optimised for implementation in cosmological simulations able to approximately resolve GMC scales ($\approx 30 - 100$ pc, see McKee & Ostriker 2007).

2.1 The internal structure of GMCs

Fragmentation of gas clouds has been intensively studied in the past, and both numerical and analytical models (e.g. Vazquez-Semadeni 1994; Kim, Ostriker & Stone 2003; Krumholz & McKee 2005; Wada 2008; Tasker & Tan 2009; Padoan & Nordlund 2011; Hennebelle & Chabrier 2011, 2013; Federrath & Klessen 2013) have shown that the density field of an isothermal, non-gravitating, turbulent gas of mean density ρ_0 is well described

by a lognormal probability distribution function (PDF). The volume-weighted PDF ($P_V(\rho)$) can be written as

$$P_V(\rho) = \frac{1}{(2\pi\sigma^2)^{1/2}} \exp \left[-\frac{1}{2} \left(\frac{\ln(\rho/\rho_0) - \langle \ln(\rho/\rho_0) \rangle}{\sigma} \right)^2 \right], \quad (1)$$

where ρ_0 is the mean cloud density and the volume-averaged value of the logarithm of the density is related to σ by $\langle \ln(\rho/\rho_0) \rangle = -\sigma^2/2$ (e.g. Ostriker, Stone & Gammie 2001; Federrath & Klessen 2013). The latter depends on the sonic Mach number (\mathcal{M}) through the following relation:

$$\sigma^2 = \ln(1 + b^2 \mathcal{M}^2), \quad (2)$$

where b parametrises the kinetic energy injection mechanism (often referred to as forcing) driving the turbulence ($b \approx 0.3 - 1$, see Molina et al. 2012). Throughout this paper we assume $b = 0.3$.

When self-gravity becomes important, the probability of finding dense regions increases and a power-law tail develops on the high-density side of the PDF. The occurrence of the power-law tail is confirmed both theoretically (e.g. Krumholz & McKee 2005; Hennebelle & Chabrier 2011; Padoan & Nordlund 2011; Federrath & Klessen 2013) and observationally via molecular line detections (e.g. Goldsmith et al. 2008; Goodman, Pineda & Schnee 2009; Schneider et al. 2016) or dust extinction measurements carried out in nearby GMCs (e.g. Kainulainen et al. 2009; Lombardi, Alves & Lada 2015; Stutz & Kainulainen 2015; Schneider et al. 2016). Treating properly the high-density tail of the density PDF is pivotal when computing the emission of high- J CO rotational lines as they have high critical densities ($n_{\text{crit}} \geq 2.9 \times 10^5 \text{ cm}^{-3}$ for $J_{\text{up}} \geq 6$) and trace the densest regions of GMCs (e.g. Carilli & Walter 2013, and references therein).

In our model we describe the time evolution of the density PDF of self-gravitating GMCs via the formalism developed by Girichidis et al. (2014). Assuming a pressure-free collapse, these authors provide a set of analytical equations to calculate the functional form of the PDF at any given time, $P_V(\rho, t)$, given the initial $P_V(\rho, 0)$. According to their model, the high-density tail of the PDF quickly asymptotes to a power law consistently with observations. Details on the calculation of $P_V(\rho, t)$ from the initial $P_V(\rho, 0)$ are given in Appendix A.

As the initial PDF, in this paper we take $P_V(\rho, 0) \equiv P_V(\rho)$, where $P_V(\rho)$ is defined in equation 1. The density at which $P_V(\rho, t)$ starts to deviate from the lognormal, ρ_{tail} , moves with time to lower densities. This is due to the fact that collapse at a given density ρ can only manifest itself after approximately a free-fall time, $t_{\text{ff}}(\rho)$ (see equation A2), implying that the collapse of lower density parcels takes a longer time. Girichidis et al. (2014) find that the tail is well defined above a density $\rho_{\text{tail}}(t)$ that evolves with time according to the following relation:

$$\frac{\rho_{\text{tail}}(t)}{\rho_0} \approx 0.2 \left(\frac{t}{t_{\text{ff}}(\rho_0)} \right)^{-2.0}. \quad (3)$$

This is the reason why (see the schematic in Fig. 1), the density PDF of a GMC is ultimately a function of two parameters: (i) the mach number (\mathcal{M}), which affects the lognormal part of the distribution; and (ii) the ratio (t/t_{ff}) – that determines the point at which the PDF significantly deviates from the lognormal distribution. Note that the additional time-dependence of the density PDF due to FUV-photoevaporation (Gorti & Hollenbach 2002; Decataldo et al. 2017; Vallini et al. 2017) is neglected in this work.

Let us now consider a GMC of radius R_{GMC} , volume $V_{\text{tot}} = 4/3\pi R_{\text{GMC}}^3$ and mean density¹ ($\rho_0 = n_0 \mu m_p$), characterized by a fixed Mach number \mathcal{M} and an evolutionary time t/t_{ff} . The normalization of the volume-weighted density PDF must satisfy the following relation:

$$V_{\text{tot}} = \int P_V(\rho|\mathcal{M}, t/t_{\text{ff}}) d\rho, \quad (4)$$

which allows us to associate to each density ρ_i a typical length-scale,

$$r_i = \left(V_{\text{tot}} \int_{\rho_i - \delta_i}^{\rho_i + \delta_i} P_V(\rho|\mathcal{M}, t/t_{\text{ff}}) d\rho \right)^{1/3} \quad (5)$$

and column density $N_i(\rho_i) = (\rho_i/\mu m_p) r_i$. The CO emission per unit volume from each density element ρ_i can be computed as follows:

$$l_{\text{CO},J}(\rho_i) = \frac{1}{V_{\text{tot}}} \varepsilon_{\text{CO},J}(n_i, N_i, Z, G_0) 4\pi r_i^2, \quad (6)$$

where $\varepsilon_{\text{CO},J}(n_i, N_i, Z, G_0)$ is the CO emissivity of the $J \rightarrow J-1$ transition as a function of the gas element (i) density, n_i ; (ii) column density, N_i ; (iii) metallicity, Z ; and (iv) **rar-ultraviolet (FUV) flux, G_0 , in the Habing band (6 – 13.6 eV) normalized to that in the solar neighbourhood ($\approx 1.6 \times 10^{-3} \text{ erg cm}^{-2} \text{ s}^{-1}$; Habing 1968).** The total CO emission² from the GMC is then

$$L_{\text{CO},J}^{\text{tot}} = \int l_{\text{CO},J}(\rho) P_V(\rho|\mathcal{M}, t/t_{\text{ff}}) d\rho. \quad (7)$$

It is useful to express equation (7) in terms of $s = \ln(\rho/\rho_0)$:

$$L_{\text{CO},J}^{\text{tot}} = \int \mathcal{L}_{\text{CO},J}(s) ds, \quad (8)$$

where $\mathcal{L}_{\text{CO},J} = l_{\text{CO},J} P_V/\rho$.

2.2 Radiative transfer

We calculate the value of $\varepsilon_{\text{CO},J}$ for the first nine rotational transitions of the CO molecule with the CLOUDY version c13.03 (Ferland et al. 2013).

CLOUDY includes ≈ 1000 reactions involving molecules containing H, He, C, N, O, Si, S and Cl atoms (see appendix A of Abel et al. 2005, for details on the molecular network). Details on the CO network including CH, CH⁺, OH, OH⁺, H₂O, H₂O⁺, H₃O⁺, O₂ and O₂⁺ are presented in Ferland, Fabian & Johnstone (1994). The majority of reaction rates come from the UMIST 2000 data base (Le Teuff, Millar & Markwick 2000). The treatment of the formation and dissociation of the H₂ molecule is outlined in Shaw et al. (2005) and it accounts for H₂ formation via gas-phase reactions and on the dust grain surface (Cazaux & Tielens 2004). The local grain properties (temperature, charge) at each point in the cloud are computed self-consistently. CLOUDY also treats the primary and secondary cosmic ray (CR) ionization processes. We adopt the default CLOUDY prescriptions for the CR ionization rate background (ζ_{CR} ; CRIR, hereafter) $\zeta_{\text{CR}} = 2 \times 10^{-16} \text{ s}^{-1}$ (Indriolo et al. 2007). The H₂ secondary ionization rate is $= 4.6 \times 10^{-16} \text{ s}^{-1}$ (Glassgold & Langer 1974). As the CRIR is a fundamental parameter that may

¹ Unless otherwise stated we consider a mixture of neutral hydrogen and helium characterized by a mean molecular weight $\mu = 1.4$

² Our treatment implicitly assumes that the each clump is exposed to the same imposed external FUV flux. This assumption neglects possible radiation anisotropies depending on the position of the clump within the GMC and shadowing effects (see appendix A of Vallini et al. 2017).

have strong effects on the gas temperature and chemical composition at high densities, we discuss the impact of our assumption on the CO luminosity inferred with our model in Appendix B.

We adopt a 1D geometry, assuming a gas slab of density n , and fixed metallicity Z . The spectral energy distribution (SED) of the radiation field impinging on the slab surface is calculated using the stellar population synthesis code `STARBURST99` (Leitherer et al. 1999), assuming a Salpeter Initial Mass Function in the range $1 - 100 M_{\odot}$, and considering a continuous star formation mode with an age of the stellar population of 10 Myr. We adopt the Geneva standard evolutionary tracks (Schaller et al. 1992) with metallicity $Z_{*} = 1 Z_{\odot}$, $0.2 Z_{\odot}$, $0.05 Z_{\odot}$, and Lejeune–Schmutz stellar atmospheres which incorporate plane-parallel atmospheres and stars with strong winds (Schmutz, Leitherer & Gruenwald 1992; Lejeune, Cuisinier & Buser 1997). The SED is normalized so that the Habing flux varies in the range $G_0 = 10^0 - 10^{4.5}$.

We adopt the gas-phase abundances ($C/H = 2.51 \times 10^{-4}$, $O/H = 3.19 \times 10^{-4}$, $N/H = 7.94 \times 10^{-5}$, $S/H = 3.24 \times 10^{-5}$)³ provided in `CLOUDY` for the ISM of the Milky Way. The abundances are an average of those measured in the cold and warm diffuse phases of the galactic ISM by Cowie & Songaila (1986) and Savage & Sembach (1996).

We implement the Weingartner & Draine (2001) grain size distribution (dn_{gr}/da ; GSD) which has been shown to reproduce (among others) the SMC extinction curve. This study provides a set of analytical equations (see equations 4–6 and the best-fitting parameters in their table 3) that (i) imposes a smooth cutoff for sizes greater than a threshold a_c , (ii) controls the steepness of this cutoff; and (iii) allows for a change in the slope ($d \ln n_{\text{gr}}/d \ln a$) below a_c .

As we are interested in obtaining predictions on the CO luminosity in high- z galaxies, we set the floor temperature of our *fiducial* simulations to that of CMB at $z = 6$, i.e. $T_{\text{CMB}} = 2.73(1 + z)\text{K} = 19.1\text{K}$. The line emission from molecular gas is affected in two ways by the CMB: (i) the higher T_{CMB} leads to an increase of the line excitation and thus of the line luminosities; and (ii) the background against which the line is measured also increases (e.g. Obreschkow et al. 2009; da Cunha et al. 2013). To test the behaviour of our model on local observations and to study the impact of the CMB temperature on our predictions, we run also a set of cases using the present-day CMB temperature, $T_{\text{CMB}} = 2.73\text{K}$ (see Section 3.2 for a discussion on this point).

We run a total of 500 ($10 \times 10 \times 5$) `CLOUDY` simulations varying (in 0.5 dex steps) $\log(n/\text{cm}^{-3})$ in the range $[1.5, 6]$, $\log G_0$ in $[0, 4.5]$ and $\log(Z/Z_{\odot})$ in $[-2, 0]$, scaling the gas-phase abundances and the dust-to-gas ratio with the metallicity of each specific model.

Such parameter space brackets the plausible range of GMC parameters relevant to high- z galaxies. The code computes the radiative transfer through the slab up to a hydrogen column density $N_{\text{H}} = 10^{23}\text{cm}^{-2}$. This stopping criterion is chosen to fully sample the molecular part of the illuminated slab, typically located at $N_{\text{H}} \gtrsim 2 \times 10^{22}\text{cm}^{-2}$ (McKee & Ostriker 2007). The output of each run is the CO line emissivity of each $J \rightarrow J - 1$ transition:

$$\varepsilon_{\text{CO},J} = \varepsilon_{\text{CO},J}(n_i, N_i, Z, G_0), \quad (9)$$

which enters in equation (6) and hence in equation (7).

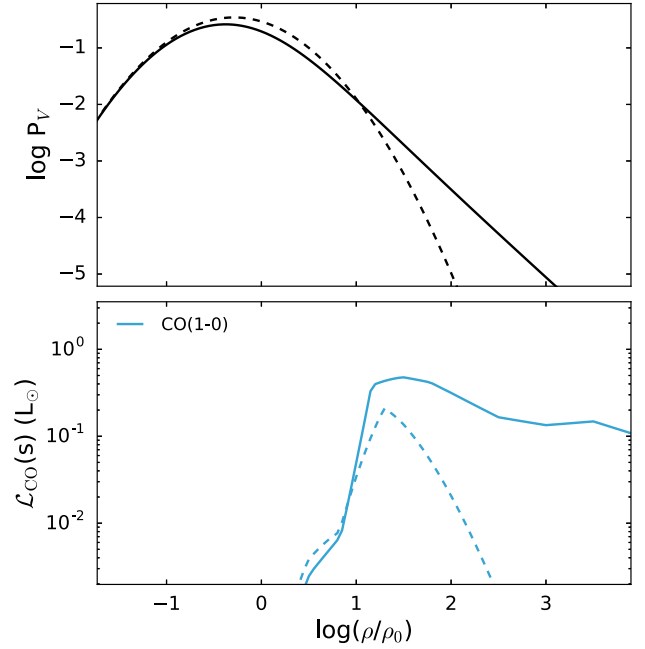


Figure 2. Upper panel: initial lognormal volume-weighted density PDF (dashed line, $\mathcal{M} = 5$), and the evolved density PDF (lognormal+tail hereafter, solid) after $t/t_{\text{ff}}(\rho_0) = 0.4$. Lower panel: specific CO(1–0) luminosity for the initial (dashed) and evolved (solid) cases shown in the upper panel.

Table 1. Parameters of the fiducial GMC.

$R_{\text{GMC}}/(\text{pc})$	$n_0/(\text{cm}^{-3})$	$\rho_0/(\text{g cm}^{-3})$	$M_{\text{GMC}}/(M_{\odot})$	$\log(Z/Z_{\odot})$	$\log G_0$
15	100	2.34×10^{-22}	4.9×10^4	0	2

3 MODEL VALIDATION

By adopting the procedure described in the previous sections we compute the luminosity of the first nine CO rotational transitions. The link between the time evolution of the density PDF, and the resulting CO luminosity is illustrated in Fig. 2. In the upper panel, we plot volume-weighted density PDF at $t = 0$ (lognormal, $\mathcal{M} = 5$) and the resulting P_V after $t/t_{\text{ff}}(\rho_0) = 0.4$ (solid line). We choose $t/t_{\text{ff}}(\rho_0) = 0.4$ to maximize the mass (97 per cent of the total mass of the GMC, Girichidis et al. 2014) in the tail, hence highlighting more clearly the effect of the tail appearance on the CO emission. The *fiducial cloud* (see Table 1) is characterized by: $n_0 = 100\text{cm}^{-3}$ ($\rho_0 = 2.3 \times 10^{-22}\text{g cm}^{-3}$), $R_{\text{GMC}} = 15\text{pc}$, $\log(Z/Z_{\odot}) = 0$ and illuminated by a FUV field with $\log G_0 = 2$. In the lower panel we plot the corresponding $\mathcal{L}_{\text{CO}}(s)$ [see equation (8)] at $t = 0$ (solid lines) and at $t/t_{\text{ff}} = 0.4$ (dashed lines). The CO(1–0) emission is boosted at high densities, once the tail has developed at $t/t_{\text{ff}} = 0.4$.

3.1 The $M_{\text{vir}} - L'_{\text{CO}}$ relation

Studies of resolved molecular clouds find that GMCs are in approximate virial equilibrium, (e.g. Larson 1981; Solomon et al. 1987; Bolatto et al. 2008) and, because of that, they obey scaling relations, often referred to as *Larson laws*. Those relations ultimately link the size (R), the velocity dispersion (σ) and the CO luminosity (L'_{CO})⁴

⁴ L'_{CO} (in $\text{K km s}^{-1} \text{pc}^2$) is linked to L_{CO} , (in L_{\odot}) through the following relation: $L_{\text{CO}} = 3 \times 10^{-11} \nu_r^3 L'_{\text{CO}}$, where ν_r is the rest frequency of the line expressed in GHz (Carilli & Walter 2013).

³ For the complete list of the abundances please refer to Ferland et al. (2013) and to the `CLOUDY` manual Hazy I.

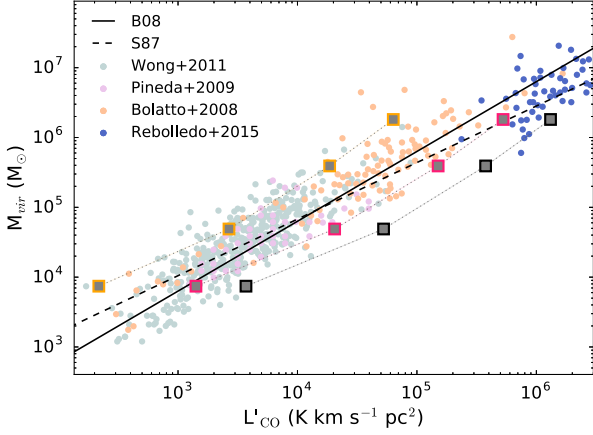


Figure 3. CO(1-0) luminosity versus virial mass of the GMC. The black dashed line is the $M_{\text{vir}}-L'_{\text{CO}}$ relation derived by Solomon et al. (1987), while the black solid line represents the relation found by Bolatto et al. (2008). The observational data concerning GMCs in nearby galaxies are plotted with coloured points. The orange points represent the compilation by Bolatto et al. (2008) including M31, M33 and nine dwarf galaxies. High-resolution observations of GMCs in the LMC by Pineda et al. (2009) are plotted with pink points, while LMC data by Wong et al. (2011) are indicated with green points. Recent GMCs/molecular complex observations in NGC6946, NGC628 and M101 by Rebolledo et al. (2015) are plotted with blue points. The $M_{\text{vir}}-L'_{\text{CO}}$ relation resulting from our model is plotted with orange ($Z = 0.1 Z_{\odot}$), magenta ($Z = 0.5 Z_{\odot}$) and black ($Z = 1 Z_{\odot}$) squares, respectively.

of GMCs (Solomon et al. 1987):

$$\begin{aligned} \sigma &\approx 0.7 R^{0.5} \text{ km s}^{-1} \\ L'_{\text{CO}} &\approx 130 \sigma^5 \text{ K km s}^{-1} \text{ pc}^2 \\ L'_{\text{CO}} &\approx 25 R^{2.5} \text{ K km s}^{-1} \text{ pc}^2. \end{aligned} \quad (10)$$

These relations are valid under the assumption that molecular gas is dominating the mass enclosed in the cloud radius and therefore the virial mass (M_{vir}) is a good measure of the H_2 traced by CO .⁵

The virial equilibrium implies that $\sigma^2 \approx GM_{\text{vir}}/R$, thus equation (10) translates into the following:

$$M_{\text{vir}} \approx 39 L'^{0.81}_{\text{CO}} M_{\odot}, \quad (11)$$

where we note that the slope of the mass-luminosity relation, $\gamma = 0.81$, is the one found by Solomon et al. (1987). Subsequent studies (e.g. Bolatto et al. 2008; Bolatto, Wolfire & Leroy 2013, and references therein) have confirmed that $\gamma \approx 1$.

In Fig. 3 we plot $M_{\text{vir}} - L'_{\text{CO}}$ as resulting from our model. More precisely, we calculate the CO(1-0) luminosity fixing the mass (M_{GMC}), radius (R_{GMC}), considering the P_V at $t/t_{\text{ff}}=0.1$, i.e. when ≈ 50 percent of the GMC mass is in the PDF tail and the rest in the lognormal distribution. The Mach number is selected so that it satisfies the following condition:

$$\mathcal{M}_s = \sqrt{\frac{GM_{\text{GMC}}}{R_{\text{GMC}}}}. \quad (12)$$

We set the sound speed of the GMC to $c_s(T = 10 \text{ K}) \approx 0.3 \text{ km s}^{-1}$. For the RT we adopt the CLOUDY runs at $z = 0$ (i.e. those with $T_{\text{CMB}} = 2.73 \text{ K}$) for different metallicities $Z = 1, 0.5, 0.1 Z_{\odot}$. Our

⁵ $M_{\text{vir}} = M_{\text{H}_2}$ implies $f_{\text{H}_2} \approx 1$. In Appendix C we compute f_{H_2} as a function of \mathcal{M} , G_0 , Z and n_0 . We show that $f_{\text{H}_2} \approx 1$ for a major fraction of the parameter space covered in this study.

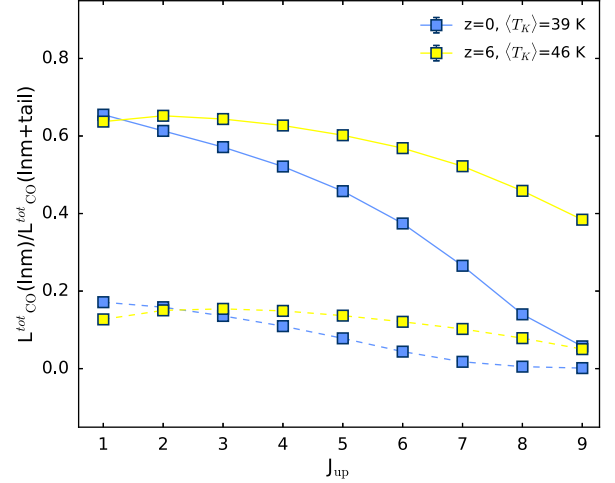


Figure 4. Ratio of the total luminosity ($L_{\text{CO}}^{\text{tot}}$) of the first nine CO rotational transitions for the fiducial GMC (see Table 1) at $t = 0$ (i.e. for a lognormal P_V) to that including the density PDF power-law tail at $t/t_{\text{ff}}(\rho_0) = 0.1$. Solid (dashed) lines represent the results obtained for a GMC characterized by $\mathcal{M} = 10$ ($\mathcal{M} = 5$), located at different redshift, $z = 0, 6$, (blue/yellow, respectively). The mean kinetic temperature at $N_{\text{H}} > 10^{21.5} \text{ cm}^{-2}$ of the GMC at $z = 0$ is $\langle T_K \rangle = 39 \text{ K}$, while at $z = 6$ is $\langle T_K \rangle = 46 \text{ K}$.

results are in nice agreement with observations, and a linear fit between $\log(L'_{\text{CO}})$ and $\log(M_{\text{vir}})$ returns a slope $\gamma = 0.96, 0.92, 0.93$ for $Z = 1, 0.5, 0.1 Z_{\odot}$, respectively. The CO luminosity decreases with decreasing Z at fixed M_{vir} , implying that the CO-to- H_2 conversion factor (see Section 4.4) increases for lower Z , as noticed also by e.g. Wolfire, Hollenbach & McKee (2010); Glover & Mac Low (2011); Narayanan et al. (2012); Bolatto, Wolfire & Leroy (2013). The model results at $Z = 0.5, 0.1 Z_{\odot}$ enclose the observations by Pineda et al. (2009); Wong et al. (2011) of GMCs in the LMC ($Z_{\text{LMC}} \approx 0.5 Z_{\odot}$ Rolleston, Trundle & Dufton 2002; Chevance et al. 2016; Lee et al. 2016).

3.2 The impact of the high-density tail

In this Section we discuss how the high-density power-law tail affects the luminosity of the various CO transitions. To do that we compare the pure lognormal density field for the fiducial GMC ($L_{\text{CO}}^{\text{tot}}(\text{lnm})$) and a distribution which includes the power-law tail after $t/t_{\text{ff}}(\rho_0) = 0.1$ ($L_{\text{CO}}^{\text{tot}}(\text{lnm} + \text{tail})$).

In Fig. 4 we plot the ratio $R_{\text{CO},J} = L_{\text{CO}}^{\text{tot}}(\text{lnm})/L_{\text{CO}}^{\text{tot}}(\text{lnm} + \text{tail})$ as a function of the upper rotational quantum number J_{up} . We separately address the case $T_{\text{CMB}}(z = 0)$ and $T_{\text{CMB}}(z = 6)$, and we assume two different values for the Mach number ($\mathcal{M}=10, 5$). In all cases, and for all the rotational transitions, $R_{\text{CO},J} < 1$. More precisely, for $\mathcal{M}=5$ the pure lognormal density distribution can account only for ≈ 20 per cent – 10 per cent ($J_{\text{up}} = 1 - 9$) of the CO emission model including the tail. If $\mathcal{M}=10$, $R_{\text{CO},J} \approx 60$ per cent – 10 per cent ($J_{\text{up}} = 1 - 9$, $z = 0$) and $R_{\text{CO},J} \approx 60$ per cent – 40 per cent ($J_{\text{up}} = 1 - 9$, $z = 6$). Both at $z = 0$ and $z = 6$, we note a clear decreasing trend of $R_{\text{CO},J}$ with J_{up} , highlighting the strong contribution of the dense tail gas to the high- J lines that have increasingly high excitation temperatures and critical densities (Carilli & Walter 2013). Hence, for a given density distribution, the emission from high- J CO lines is boosted for warmer kinetic temperatures.

This is exactly what we obtain at fixed Mach numbers, where the drop of $R_{\text{CO},J}$ at high- J transitions is steeper at $z = 0$ than at $z = 6$. This is because the mean kinetic temperature of the molecular gas

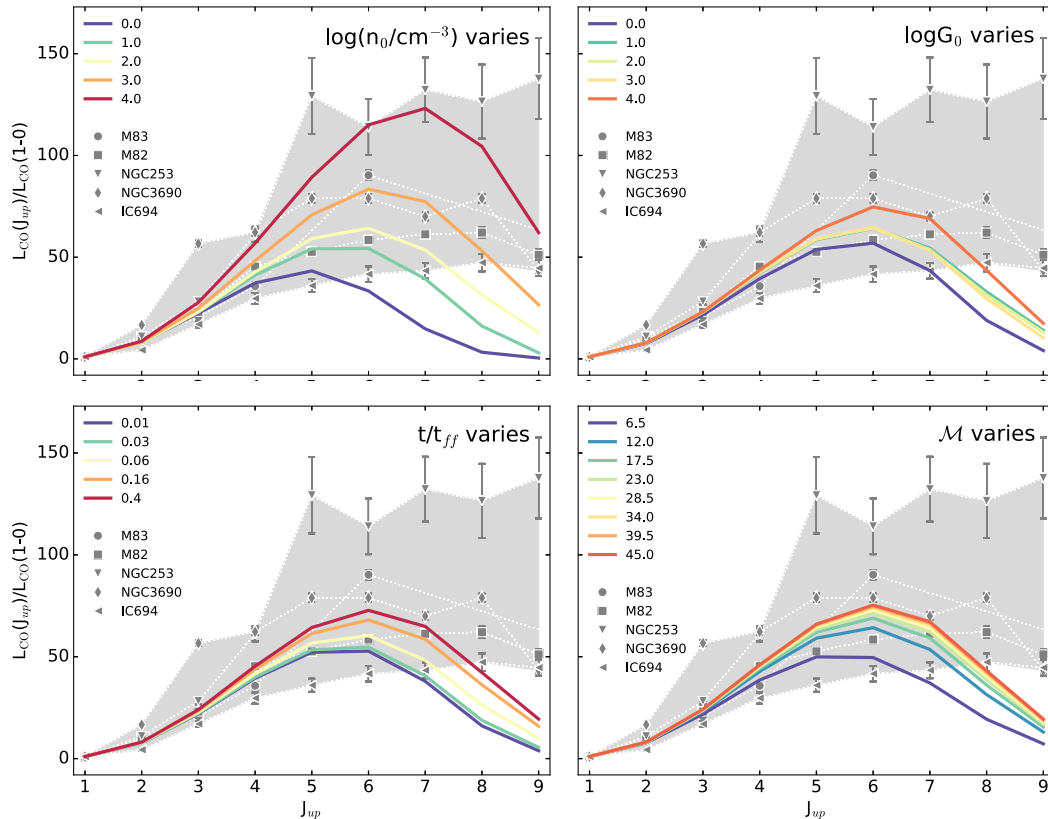


Figure 5. The coloured solid lines represent the CO SLEDs, normalized to the CO(1–0) transition, obtained from our modelling at $z = 0$, when varying n_0 , G_0 , t/t_{ff} and \mathcal{M} (top-left, top-right, bottom-left, bottom-right panels, respectively). The shaded region highlights the variation of the observed CO SLEDs for starburst galaxies in the nearby Universe (Mashian et al. 2015).

(i.e. for $N_H > 10^{21.5} \text{ cm}^{-2}$) is lower at $z = 0$ ($\langle T_K \rangle = 39 \text{ K}$) than at $z = 6$ ($\langle T_K \rangle = 46 \text{ K}$). The increase of the Mach number from $\mathcal{M}=5$ to $\mathcal{M}=10$ boosts $R_{CO,J}$, i.e. the emission of the lognormal-distributed gas. The reason is that for large Mach numbers the lognormal distribution becomes wide [equation (2)] and hence a non-negligible fraction of the gas is compressed in high density, albeit not in gravitationally bound, structures. Such turbulent density enhancements are transient and might not survive long enough time to allow formation of CO and H_2 molecules (see later in Section 4.3).

3.3 The CO SLED

Observations of the CO SLEDs can be used as a tool to constrain the properties of molecular gas and to link them to the star formation process, both from single GMCs (e.g. Pon et al. 2016; Lee et al. 2016; Indriolo et al. 2017) and on galactic scales (e.g. Rosenberg et al. 2015; Mashian et al. 2015; Lu et al. 2017; Pozzi et al. 2017). Any model that aims at predicting and interpreting the CO emission must be able to reproduce the relative strength of the various lines under different ISM conditions. In Fig. 5 we investigate how the resulting CO SLED from the fiducial cloud (Table 1) is influenced by variations of (i) the mean density, n_0 , (top left) is influenced by variations of (ii) FUV Habing flux, G_0 , (top right) and the density PDF shape parametrized by (iii) t/t_{ff} (bottom left) and \mathcal{M} (bottom right). Given that we will compare our results with local observations of starburst galaxies in the local Universe (Mashian et al. 2015), in this Section we adopt CLOUDY runs with present-day CMB temperature. For the

reasons explained later, we finally analyse the effects of metallicity variations separately.

3.3.1 Mean density effect

As already mentioned in Section 1 different CO rotational transitions trace gas with different properties. While low- J rotational transitions ($J_{up} \leq 3$) arise from diffuse ($n = 10^2 - 10^4 \text{ cm}^{-3}$), cold ($T_K = 10 - 20 \text{ K}$) molecular ISM, higher- J transitions are excited in denser ($n = 10^5 - 10^6 \text{ cm}^{-3}$) and warmer ($T_K = 50 - 600 \text{ K}$) gas (Kaufman et al. 1999). In Fig. 5 we plot the resulting CO SLEDs, normalized to the CO(1–0) transition, for different mean density n_0 ; the values of the other parameters are kept fixed to the fiducial ones. As expected, the peak of the CO SLED rise and shifts from $J_{up} = 5 \rightarrow 7$ with increasing n_0 .

This does not come as a surprise, as the population of high- J CO levels – set by the competition of collisional excitation and radiative de-excitation – increases with increasing mean gas density. This eventually boosts the emission of high- J CO lines, and shifts the peak of the CO SLED towards larger J (see e.g. Weiß et al. 2007; da Cunha et al. 2013; Narayanan & Krumholz 2014).

3.3.2 FUV radiation effect

For high- J CO lines, large gas temperatures are required to populate the corresponding rotational levels. An increase of the FUV fluxes at the GMC surface produces warmer gas and can ultimately boost

the peak of the normalized CO SLED. Recall that CO(1–0) traces gas that is colder than that in which high- J CO lines are excited. Note however that, in spite of a large (four dex) variation in G_0 , the CO SLED peak increases only by ≈ 1.5 times (upper right panel of Fig. 5). As emphasized also by Kaufman et al. (1999), the temperature in the CII/CI/CO transition layer – directly influencing the CO emission – has a weak dependence on the Habing flux. A larger G_0 also forces such boundary to move deeper in the cloud.

3.3.3 Density PDF shape effects

In the lower left panel of Fig. 5 we plot the CO SLED dependence on the cloud evolutionary time t/t_{ff} . As discussed in Fig. 4, the emergence of the high-density tail in the more evolved stages boosts the emission of all CO lines and more noticeably of the high- J ones. This explains the shift-and-increase effect of the CO SLED peak at larger t/t_{ff} . A similar effect is also produced by large Mach numbers (lower right panel). As already explained a larger \mathcal{M} causes an increase in the standard deviation of the lognormal density distribution, thus allowing the gas to achieve larger densities with a non-negligible probability. This ultimately enhances the emission of high- J CO lines.

For comparison, in Fig. 5 we plot in grey the range covered by the observed CO SLEDs (up to $J_{\text{up}} = 9$) of five nearby starburst galaxies extracted from the sample of Mashian et al. (2015). We do not expect that any of our single cloud model can, alone, reproduce the observed CO SLED on global galactic scales. In fact, the galaxy-integrated CO SLEDs results from the overlap of many different GMCs, which have different illumination, density and temperature conditions.

Nevertheless the comparison of our simulated CO SLEDs with those observed allows us to highlight three points:

- (i) Even though it is out of our scope to reproduce in detail the CO SLED shapes of the galaxies in the sample, the predictions for $J_{\text{up}} \leq 6$ reproduce well the observed trends.
- (ii) The model underpredicts the luminosity of $J_{\text{up}} \geq 7$ lines. This does not come as a surprise, as we have not included shocks in our treatment. Shocks in GMCs are known (Pon, Johnstone & Kaufman 2012; Pon et al. 2015, 2016) to dissipate their energy primarily through CO rotational transitions. In particular, $J_{\text{up}} \geq 7 - 8$ lines come often from shocked gas and are typically brighter than those predicted by PDR models.
- (iii) Our model assumes a fixed CRIR and this might affect the shape of the CO SLED. For example, the CO SLED of NGC 253, in which the CRs flux is 100 – 1000 times the MW one (Bradford et al. 2003), is not reproduced by any combination of parameters shown in Fig. 5. In Appendix B we address in detail the effect of the CRIR variation on the CO line luminosity.

3.3.4 Metallicity effect

The analysis of the CO SLED presented in Fig. 5 has been performed at solar metallicity, as we were comparing our results with observations of local starburst galaxies whose $Z \approx Z_{\odot}$. This is likely not the case of high- z sources ($Z < Z_{\odot}$ Pallottini et al. 2014), which are the primary targets of this work. In what follows we will discuss the impact of Z variations on the CO SLEDs and we will use the observations of multiple CO emission lines in the N159W region of the Large Magellanic Cloud (LMC) (Lee et al. 2016) as benchmark.

N159W is one of the three prominent GMCs ($M_{\text{H}_2, \text{N159W}} \approx 10^5 M_{\odot}$ Fukui et al. 2015) in the N159W complex in the LMC

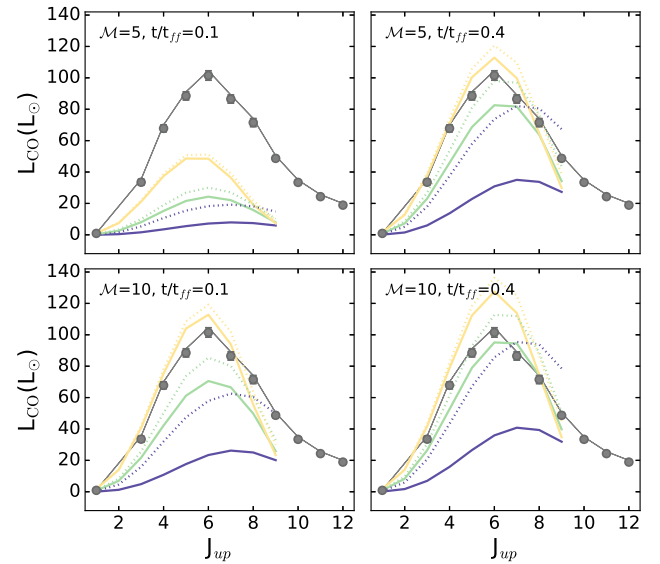


Figure 6. The combined effect of the variation of $Z = 0.1, 0.5, 1 Z_{\odot}$ (purple, green, yellow lines, respectively) and $\log G_0 = 2, 1.5$ (dotted, solid lines) on the CO SLED. We consider four different models characterized by $\mathcal{M} = 5, 10$ (upper and lower row, respectively), and $t/t_{\text{ff}} = 0.1, 0.4$ (left and right columns, respectively). The grey points represent the observed CO line emission from the N159W GMC in the LMC (Lee et al. 2016).

($d_{\text{LMC}} \approx 50$ kpc, Schaefer 2008), whose physical conditions have been extensively studied at multiple wavelengths (Lee et al. 2016, and references therein). Recently, Lee et al. (2016) presented a coherent analysis of the CO and fine structure ([CII] 158 μm , [OI] 145 μm , [CI] 370 μm) line emission to assess the properties of the molecular gas in N159W. N159W is a perfect target to test our model at low metallicities for two reasons: (i) the size⁶ of the observed region (≈ 150 arcsec corresponding to ≈ 35 pc) is comparable to the diameter of our fiducial GMC (30 pc); and (ii) Lee et al. (2016) performed a PDR and shock analysis of N159W CO SLED up to the CO(12–13) transition with which we will compare our results.

In Fig. 6 we plot the CO SLED as a function of Z assuming two different FUV fluxes at the GMC surface ($\log G_0 = 1.5, 2$). We note that the luminosity of all CO lines decreases with Z . The effect of the G_0 variation (solid and dotted lines in Fig. 6) is negligible at $Z = Z_{\odot}$, but it increases at lower metallicities. This is because, as pointed out by e.g. Chevance et al. (2016), a low metal (and dust) abundance results in less shielding. The FUV photons penetrate deeper into the cloud producing thicker PDRs and smaller CO cores. In Fig. 6 we show that there is a positive correlation between L_{CO} , \mathcal{M} and/or t/t_{ff} . This is in line with what was discussed in the previous sections for the $Z = Z_{\odot}$ runs. In their PDR analysis of metal FIR lines, Lee et al. (2016) found that the best-fit is obtained for $\log G_0 \approx 1.8 - 2.1$. Moreover, from the study of the CO-traced molecular gas they conclude that $T_{\text{K}} = 153 - 754$ K and $n_{\text{H}_2} \approx 10^3$. The PDR models used in their analysis, however, fail to explain the CO observations. Their conclusion is that the CO-emitting gas is excited by something other than UV photons, possibly shocks. Our

⁶ The area of the map in Fig. 8 of Lee et al. (2016) is $\approx 150 \times 150 \text{ arcsec}^2$. Note, however, that this must be considered as an upper limit on the area of the region from which the CO emission is observed. In fact, only those pixel for which the S/N > 5 were considered by Lee et al. (2016) when computing the total luminosity quoted in their table 3.

model, including the internal density structure of the GMC is instead successful in matching the data. In fact, we find that models with $Z = 0.5 Z_{\odot}$ and $\log G_0 = 1.5$ can reproduce the CO SLED up to $J_{\text{up}} = 8$ if $\mathcal{M}=10$ and $t/t_{\text{ff}}=0.4$.

4 GALAXY SIMULATIONS

We apply the above CO-emission model to post-process a recently produced zoom-in simulation described in Pallottini et al. (2017a). Below we briefly summarize its main features.

Starting from cosmological initial conditions, we have used a modified version of the Adaptive Mesh Refinement code RAMSES (Teyssier 2002) to carry out a zoom-in simulation of a $z \sim 6$ dark matter (DM) halo of mass $\sim 10^{11} M_{\odot}$. In the zoomed-in region the gas has mass resolution of $10^4 M_{\odot}$, and dynamics is followed down to spatial scales of $\simeq 30$ pc. Stars are formed from molecular hydrogen, whose abundance is computed on the fly using the non-equilibrium chemistry code KROME (Grassi et al. 2014), which is conveniently coupled to our customised version of RAMSES. The thermal and turbulent energy content of the gas is modelled following Agertz & Kravtsov (2015). As detailed in Pallottini et al. (2017b), stellar feedback includes supernovae, winds from massive stars and radiation pressure. Stellar energy inputs and chemical yields depend both on time and stellar populations; the feedback prescription accounts for energy losses inside the GMC (albeit the density structure modelling introduced here has not yet been included).

The selected DM halo hosts ‘Althæa’, a galaxy characterized by a stellar mass $M_{\star} \sim 10^{10} M_{\odot}$, a mean gas surface density $\langle \Sigma_{\text{gas}} \rangle = 220 M_{\odot} \text{ yr}^{-1}$, and a SFR $\sim 100 M_{\odot} \text{ yr}^{-1}$ at $z \sim 6$. Althæa features a SFR-stellar mass relation compatible with observations (e.g. Jiang et al. 2016), is in agreement with the Schmidt–Kennicutt relation (Krumholz, Dekel & McKee 2012), and has a $[\text{C II}]$ emission $\log(L_{\text{CII}}/L_{\odot}) \simeq 8.3$, slightly lower than the one expected from the local $[\text{C II}]$ -SFR relation (De Looze et al. 2014) and compatible with some high- z galaxy upper-limits (Schaerer et al. 2015).

4.1 Luminosities of individual simulated clouds

As outlined in Fig. 1, and discussed in Section 2, our CO model needs t/t_{ff} , \mathcal{M} , n_0 , R_{GMC} , G_0 and Z as inputs. In Fig. 7 we plot the H_2 mass weighted PDF of \mathcal{M} – n_0 relation in Althæa, considering a $z = 6$ snapshot of the simulation. In Althæa the density PDF peaks at $n_0 \approx 300 \text{ cm}^{-3}$. In addition there is a small fraction of very dense gas ($n_0 > 1000 \text{ cm}^{-3}$) – the low \mathcal{M} diagonal stripe. This part of the PDF describes the virtually metal-free gas in which H_2 production proceeds via gas-phase reactions rather than on dust grain surfaces and can survive only if self-shielded by a high density. The Mach number has a relatively wide distribution (see the inset of the Figure) with a pronounced peak at $\mathcal{M} \approx 30$. This high level of turbulence is mostly supported by momentum injection associated with radiation pressure on to dust around massive stellar clusters and supernova explosions. It is a consequence of the very high star formation rate per unit area which in Althæa is about 1000 times higher than in the Milky Way. To guide the following interpretation, in Fig. 8 we plot as a function of Z and G_0 the luminosity of the brightest transition (indicated by the white contours) from a single GMC characterized by $\mathcal{M} = \langle \mathcal{M} \rangle_{\text{Althæa}} = 30$ and $n_0 = \langle n_0 \rangle_{\text{Althæa}} = 300$. Considering that $\langle Z \rangle_{\text{Althæa}} = 0.5 Z_{\odot}$ and $\langle G_0 \rangle_{\text{Althæa}} = 100$, we expect a typical $L_{\text{CO}(7-6)} \approx 10^2 L_{\odot}$ from such a cloud, which has a mass of $1.4 \times 10^5 M_{\odot}$. The CO SLED peaks at CO(7–6) transition for all Z if $\log G_0 < 1.5$, otherwise, if $\log G_0 > 1.5$ the peak shifts towards higher J_{up} with decreasing metallicity.

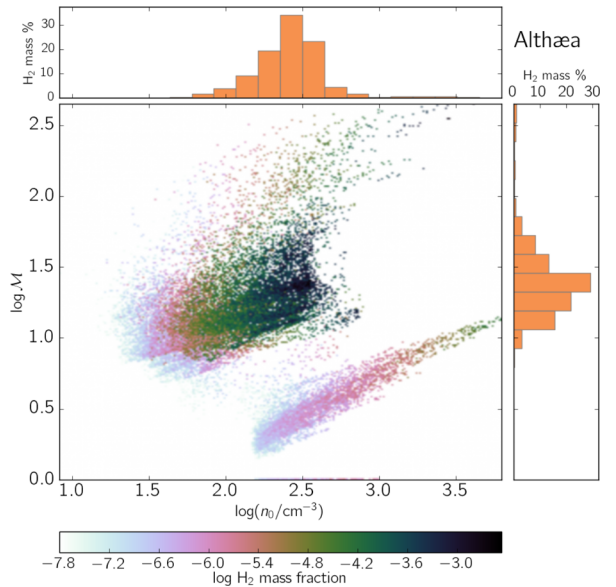


Figure 7. Mach number versus density in Althæa at $z = 6$. The relation is plotted using the H_2 mass weighted PDF. The projections on the n (\mathcal{M}) axis are shown as horizontal (vertical) insets.

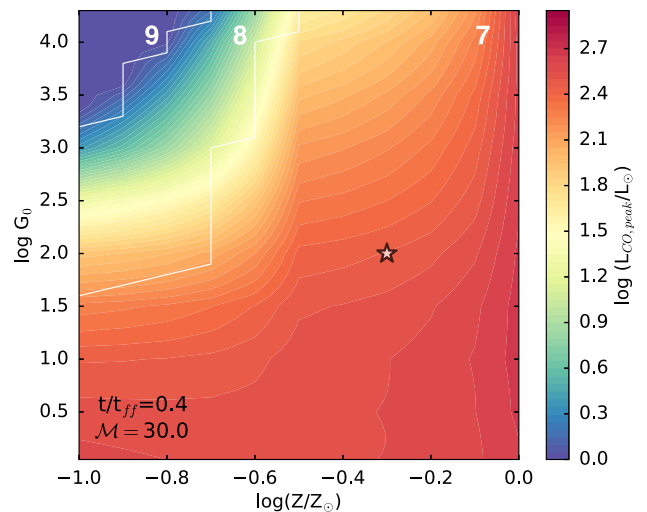


Figure 8. Luminosity of the CO transition at peak of the CO SLED (J_{up} indicated on the contours) as a function the G_0 and Z . The contours are obtained for $t/t_{\text{ff}} = 0.4$ assuming $\mathcal{M} = 30$ and $n_0 = 300 \text{ cm}^{-3}$.

4.2 CO emission from Althæa

Fig. 9 shows the morphology of the CO(1–0) and CO(7–6) emission in Althæa. We select these two lines among all the CO rotational transitions because: (i) the CO(1–0) enters in the calculation of the CO-to- H_2 conversion factor, α_{CO} , which we will discuss in detail in Section 4.4; and (ii) the CO(7–6) is the most luminous transition of the Althæa CO SLED (see Section 4.3) and it is observable with ALMA from $z \approx 6$.

As extensively discussed in Pallottini et al. (2017a), Althæa features a clearly defined, even though rather perturbed, spiral disc of radius $\approx 0.5 \text{ kpc}$, embedded in a lower density ($n \approx 0.1 \text{ cm}^{-3}$) medium. The CO emission traces the disc where indeed most of the H_2 mass resides. Both the CO(1–0) and the CO(7–6) maps show an enhanced emission clump along the spiral arms. The peak of the CO(1–0) and CO(7–6) surface brightnesses are coincident

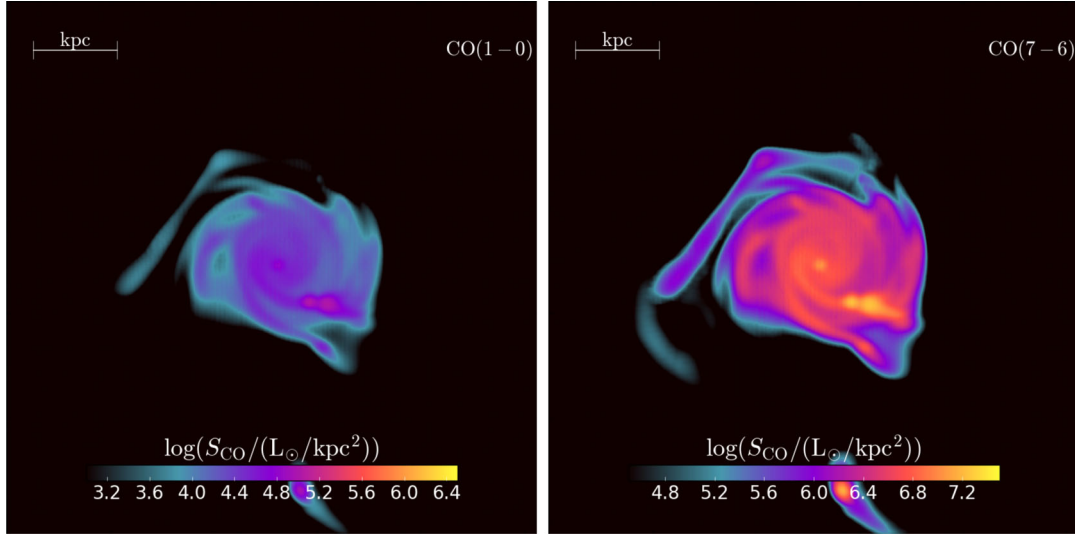


Figure 9. CO(1–0) and CO(7–6) surface brightness maps of Althæa. Note the different scale of the colour bars in the two panels.

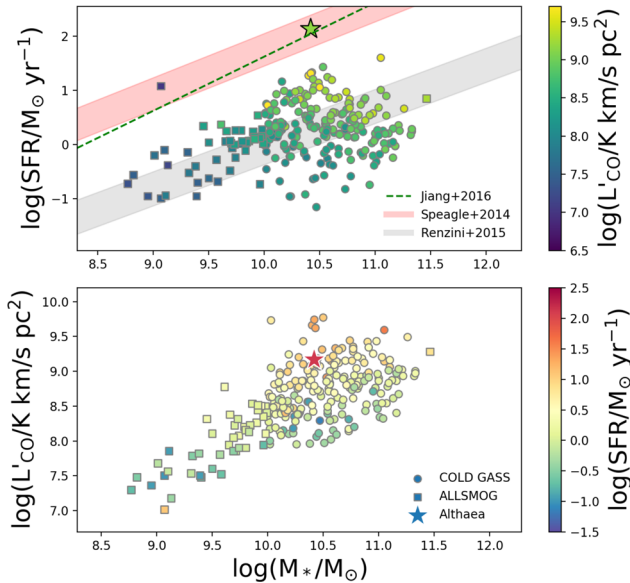


Figure 10. Upper panel: the COLD GASS (Saintonge et al. 2011) (circles) and ALLSMOG (Cicone et al. 2017) (squares) samples are plotted in the M_* –SFR plane and colour coded as a function of the CO(1–0) luminosity. The grey (red) shaded region indicates the location of the star-forming MS at $z \approx 0$ (Renzini & Peng 2015), ($z = 6$, Speagle et al. 2014); the green dashed line is the best fit obtained from observations in LBGs/LAEs at $z \approx 6$ (Jiang et al. 2016). Althæa’s position is marked with a star. Lower panel: $L'_{\text{CO}} - M_*$ relation for COLD GASS, ALLSMOG and Althæa, colour coded as a function of SFR.

($\log(S_{\text{CO}(1-0)}/L_{\odot} \text{ kpc}^{-2}) \approx 5.0$, and $\log(S_{\text{CO}(7-6)}/L_{\odot} \text{ kpc}^{-2}) \approx 7.2$, respectively). Not surprisingly, they are co-located with a high-density ($n \approx 10^3 \text{ cm}^{-3}$) clump where also the H_2 $17.03 \mu\text{m}$ and $[\text{C II}]$ lines reach their maximum surface brightness (Pallottini et al. 2017a).

To understand how the total CO(1–0) luminosity of Althæa compares with local observations, in the upper panel of Fig. 10 we plot the M_* –SFR relation for galaxies in the COLD GASS (Saintonge et al. 2011) and ALLSMOG (Cicone et al. 2017) samples, as well as the location of Althæa in the same plane. The points are colour coded in L'_{CO} . We also highlight the evolution of the star-forming

‘main sequence’ (MS) from $z = 0$ (Renzini & Peng 2015) to $z = 6$ (Speagle et al. 2014; Jiang et al. 2016).

Althæa nicely falls on the MS at $z = 6$ (Speagle et al. 2014). Its M_* –SFR relation is in agreement with that recently found by Jiang et al. (2016) in $z \approx 6$ LAEs and LBGs characterized by stellar ages > 100 Myr. As shown in the lower panel of Fig. 10, the CO(1–0) luminosity of Althæa is $L'_{\text{CO}} = 10^{9.17} \text{ K km s}^{-1} \text{ pc}^2$ ($L_{\text{CO}} = 10^{4.8} L_{\odot}$) and it is comparable to that of galaxies with the same stellar mass at $z \approx 0$.

The specific star formation rate (sSFR = SFR/M_*) of Althæa is higher than that of MS galaxies at $z = 0$, i.e. its SFR is larger than that of galaxies with comparable M_* (see the colour code of the Althæa symbol in the lower panel of Fig. 10). Therefore the CO(1–0) luminosity per unit SFR in Althæa is lower than that of $z \approx 0$ MS galaxies.

4.3 The CO SLED in Althæa

The CO SLED is a unique tool to infer the properties of molecular gas, even if the simultaneous effect of the various parameters (e.g. the gas density, the FUV field, the gas metallicity) often makes its interpretation challenging. This is the reason why, in Section 3.3, we separately discussed the effect of each of the relevant parameters entering in our modelling. Here, we will refer to the results of that analysis to interpret the CO SLED of Althæa plotted in Fig. 11.

The CO SLED of Althæa includes the effects of CMB background radiation at $z = 6$. To isolate the effects of the CMB, we have also produced a case in which the CMB temperature is fixed at its present-day ($z = 0$) value. The latter peaks at $J = 6$ and is consistent with the range spanned by the observed CO SLEDs in a sample of local starburst galaxies (Mashian et al. 2015). The higher average GMC temperature due to the warmer CMB at $z = 6$ shifts the SLED peak at $J = 7$; in addition, the galaxy is about two times more luminous in the brightest line available if located at $z = 6$ compared to the $z = 0$ case.

According to da Cunha et al. (2013) the observed flux of the J -th line (S_J^{obs}) against the CMB over the intrinsic one can be expressed as

$$\frac{S_J^{\text{obs}}}{S_J^{\text{intrinsic}}} = 1 - \frac{B_{\nu}[T_{\text{CMB}}(z)]}{B_{\nu}[T_{\text{ex}}]}, \quad (13)$$

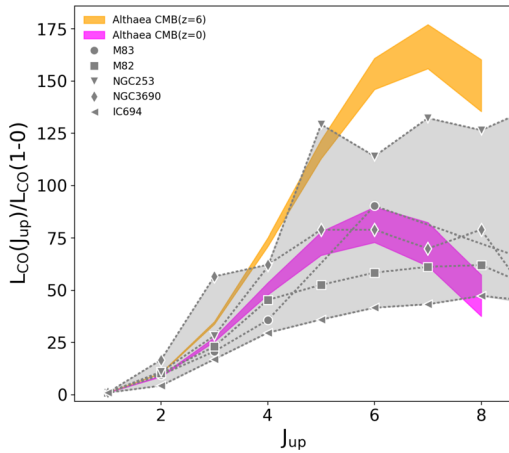


Figure 11. The CO SLED in Althaea normalized to the CO(1–0) transition. In orange we plot the actual CO SLED, while the magenta shaded region represents the CO SLED of Althaea considering the CO emission obtained with RT calculations with $T_{\text{CMB}}(z=0)$. The grey points represent the CO SLEDs of the five starburst galaxies in the Mashian et al. (2015) sample. The shaded area in the simulated SLEDs corresponds to variation of t/t_{ff} in the range [0.01, 0.4].

where ν is the rest frame frequency of the transition and B_ν is the blackbody spectrum at temperature T . Using this equation, the ratio of the observed versus intrinsic CO(7–6) flux from $z=6$ (substituting $T_{\text{CMB}}(z=6) = 19.1$ K and $T_{\text{ex}} = T_{\text{k,GMC}, z=6} = 46$ K) is ≈ 0.8 .

Then, we can estimate the ratio of the observed CO(7–6) from $z=6$ over that at $z=0$. This can be done by computing the intrinsic CO(7–6) luminosity in LTE (Obreschkow et al. 2009, see equations 4,5), using $T_{\text{ex}} = 39$ K ($T_{\text{ex}} = 46$ K) for $z=0$ ($z=6$). This yields $S_J^{\text{obs}}(z=6)/S_J^{\text{obs}}(z=0) = 0.8 S_J^{\text{int}}(z=6)/S_J^{\text{int}}(z=0) \approx 1.3$.

Qualitatively the CO(7–6) suppression due to the CMB [equation (13)] is compensated by the increased temperature of GMCs at high z . However the ratio as estimated in LTE (≈ 1.3) is slightly lower than what we find (≈ 2.3) from our model (Fig. 11). The origin of such discrepancy is due to a combination of the following factors: (i) CLOUDY calculations show that the excitation temperature inside clouds is not uniform, but has a varying spatial profile; (ii) the predicted CO luminosity in Althaea arises from a collection of emitting clouds with different densities; and (iii) the presence of an external stellar radiation field, G_0 , induces deviations from the LTE regime implicitly assumed by equation (13).

In Fig. 11 the Althaea SLEDs are represented with shaded areas, which highlight the variation of the CO line luminosity as a function of t/t_{ff} . We let t/t_{ff} vary in the range [0.01, 0.4] that causes an increase of L_{CO} by a factor ≈ 1.5 . The impact of the tail is relatively small because the average Mach number of molecular cells in the simulation is ≈ 30 (Fig. 7), which implies $\sigma \approx 2.0$ (see equation 2). In this case the median density of the mass-weighted PDF is $\rho_{50 \text{ per cent}} = n_0 \times e^{-0.14}$ (see e.g. table 1 in Girichidis et al. 2014). Given that the typical number density of molecular cells is $n_0 \approx 300 \text{ cm}^{-3}$, this means that 50 per cent of the mass actually resides in structures with densities above $\rho_{50 \text{ per cent}} = 260 \text{ cm}^{-3}$ even without including the contribution of the tail. Given that for Althaea the t/t_{ff} parameter has a minor impact on the CO luminosity, in what follows we fix $t/t_{\text{ff}} = 0.1$.

However, we re-emphasize that, as discussed in Section 3.1, this statement holds true only in chemical equilibrium, i.e. if the time-scale for H_2 (and CO) formation ($t_{\text{H}_2}^{-1} \propto \mathcal{R}n$, with $\mathcal{R} \approx$

$10^{-17} \text{ cm}^3 \text{ s}^{-1}$ Jura 1975) is shorter than the typical lifetime of turbulent density enhancements. A simple estimate can be obtained as follows. Let us consider a clump with $n = 10^3 \text{ cm}^{-3}$, corresponding to a typical scale $L_e \approx 1 \text{ pc}$ (see equation 5). At such density, the H_2 formation time-scale is $t_{\text{H}_2} \approx 10^{14} \text{ s}$ (see Liszt 2007; Glover et al. 2010, for a detailed calculation). Let us assume that the clump lifetime is the eddy turnover time ($t_e = L_e/v_e$). Using Larson’s law, we know that the turbulent velocity scales as $v_e \propto L_e^{1/3}$ hence, $v_e = \mathcal{M}c_s(L_e/(2R_{\text{GMC}}))^{1/3}$. Substituting $\mathcal{M} \approx 30$, and $c_s = 0.3 \text{ km s}^{-1}$ we obtain $t_e \approx 10^{13} \text{ s} < t_{\text{H}_2}$. This simple estimate shows that it can be difficult for H_2 (and CO) to form in a purely turbulent environment and gravitational collapse might be needed to keep the over-dense regions bound. Finite lifetime of clumps and non-equilibrium chemistry is typically not considered in CO emission calculations that explore a wide range of physical conditions (e.g. Kazandjian et al. 2016), while it is accounted for in single cloud simulations (e.g. Glover et al. 2010; Shetty et al. 2011). This is an interesting aspect that is worth to be investigated in future work.

4.4 CO-to- H_2 conversion factor

The so-called CO-to- H_2 conversion factor is defined as the ratio of the molecular gas mass to the CO(1–0) line luminosity:

$$\alpha_{\text{CO}} \equiv \left(\frac{M_{\text{H}_2}}{L'_{\text{CO}}} \right) M_\odot (\text{K km s}^{-1} \text{ pc}^2)^{-1}. \quad (14)$$

Observationally, α_{CO} is determined by combining independent measurements of H_2 gas mass with the detection of the CO(1–0) line. There are three methods to infer the molecular mass and/or column density: (1) assume that GMCs are in virial equilibrium, and derive the H_2 mass from the CO line width (e.g. Larson 1981; Solomon et al. 1987); (2) assume a constant dust-to-gas ratio and use the dust continuum emission, possibly combined to HI measurements, to infer N_{H_2} , e.g. Pineda, Caselli & Goodman (2008, in resolved Galactic GMCs) and Leroy et al. (2011); Magdis et al. (2011); Sandstrom et al. (2013, for extragalactic studies); and (3) through γ -ray emission induced by cosmic ray interactions with H_2 molecules (e.g. Padovani, Galli & Glassgold 2009). In the MW disc the conversion factor is fairly constant, $\alpha_{\text{CO}} = 4.3 \pm 1.3 M_\odot (\text{K km s}^{-1} \text{ pc}^2)^{-1}$ (Bolatto et al. 2013) on large ($\approx \text{kpc}$) scales.

In recent years, a number of observational studies have provided evidence for at least two physical regimes where α_{CO} departs from the MW value. The first deviation is observed in sources with high-surface density and/or warm molecular gas such as mergers and starburst galaxies where the conversion factor is lower than MW one (e.g. Yao et al. 2003; Tacconi et al. 2008; Papadopoulos et al. 2012). To first order high gas temperatures, and gas surface densities (Σ_{H_2}), yield brighter CO emission at fixed molecular mass, thus decreasing the conversion factor (Narayanan et al. 2011, 2012).

A deviation in the opposite direction is instead observed in low-metallicity galaxies. In these sources α_{CO} is larger than in the MW (e.g. Bolatto et al. 2008; Leroy et al. 2011). This is due to the low C and O abundances and, most importantly, to the low dust-to-gas ratios which prevent an efficient shielding against FUV dissociating photons.⁷ The reduced CO abundance then produces a fainter luminosity. The actual value of α_{CO} in high-redshift ($z \geq 6$) galaxies is far from being firmly constrained. On the one hand, high- z galaxies are more compact, dense and star-bursting than the MW; all these

⁷ We recall that, contrary to H_2 , CO cannot self-shield.

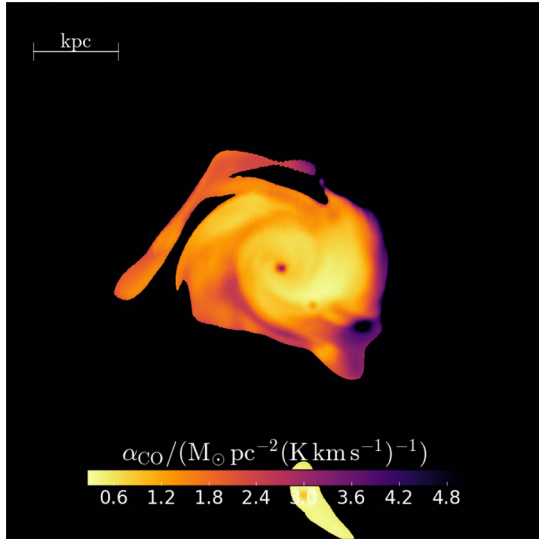


Figure 12. The map of α_{CO} in Althaea.

facts lead to lower α_{CO} values. On the other hand, if their metallicity is sub-solar, one would expect higher α_{CO} ratios.

In Fig. 12 we plot the α_{CO} map of Althaea. The map is obtained by dividing the CO(1–0) surface brightness by the corresponding H_2 mass surface density. The mass of molecular hydrogen in each cell is

$$M_{\text{H}_2, \text{cell}} = f_{\text{H}_2, \text{GMC}} M_{\text{gas, cell}}, \quad (15)$$

where $f_{\text{H}_2, \text{GMC}}$ is the molecular fraction obtained with the sub-grid model (see Appendix C for details). The mean value (standard deviation) of the CO-to- H_2 in Althaea is $\langle \alpha_{\text{CO}} \rangle = 1.54 \pm 0.9 \text{ M}_{\odot}/(\text{K km s}^{-1} \text{ pc}^2)$. Even though \mathcal{M} and n_0 have similar relative variations in the disc of Althaea, i.e. $\sqrt{\langle \mathcal{M}^2 \rangle} / \langle \mathcal{M} \rangle \approx \sqrt{\langle n_0^2 \rangle} / \langle n_0 \rangle \approx 0.2$, most of the dispersion of α_{CO} is due to the density fluctuation. The α_{CO} is rather constant through the disc and this is in agreement with what was found by Sandstrom et al. (2013) that pointed out that the radial profile of α_{CO} in spiral galaxies is mostly flat. However, Sandstrom et al. (2013) found also a slight decrease of the conversion factor towards the centre of the observed galaxies. In Althaea we do not see such a trend.

As pointed out previously, α_{CO} can be influenced by the gas surface density Σ_{H_2} , by the strength of the Habing field, by the gas metallicity Z and also by the CRIR.

Recently, Clark & Glover (2015); Glover & Clark (2016) performed detailed numerical simulations of turbulent molecular clouds that cover a wide range of metallicities, strength of the interstellar radiation field (ISRF) and cosmic ray ionization rate to investigate the impact of these parameters on the conversion factor. They find that α_{CO} increases with decreasing metallicities, in agreement with observations in the nearby Universe (e.g. Bolatto et al. 2008; Leroy et al. 2011). Increasing the ISRF and the CRIR produces different effects on the well-shielded clumps, where CO survives effectively, and in the diffuse interclump medium, where CO is instead dissociated effectively. Hence, even for high values of the ISRF, the integrated intensity from dense clumps increases owing to the heating of the gas. This is especially relevant in the case of model clouds characterized by high-density and high turbulent velocity dispersion, for which the conversion factor drops close to the MW value, even when the local ISRF is 100 times the fiducial (i.e. $G_0 = 1.7$) value.

The warm temperature of the molecular gas, sustained by the CMB at $z = 6$, and the high level of turbulence and gas surface densities of Althaea, are likely the two main reasons pushing the Althaea CO-to- H_2 conversion factor below that of the MW, despite the sub-solar metallicity, $\langle Z \rangle = 0.5 Z_{\odot}$ and $\text{SFR} \approx 100 \text{ M}_{\odot} \text{ yr}^{-1}$ featured by Althaea. As a caveat, we also note that in our model we totally neglect any type of stellar feedback on GMCs (e.g. Gorti & Hollenbach 2002; Decataldo et al. 2017; Vallini et al. 2017), which may affect the density field of GMCs, and ultimately increase the conversion factor.

Finally, we compare our inferred conversion factor with the one resulting from the best-fitting formula, $X_{\text{CO}}/(\text{cm}^2 \text{ K km s}^{-1}) = 6.3 \times 10^{19} \alpha_{\text{CO}}/(\text{M}_{\odot} \text{ K km s}^{-1} \text{ pc}^2)$, obtained by Narayanan et al. (2012). They simulate the hydrodynamic evolution of both isolated and merging disc galaxies finding that $X_{\text{CO}} = (1.3 \times 10^{21})(Z/Z_{\odot})^{-1}(\Sigma_{\text{H}_2}/(\text{M}_{\odot} \text{ pc}^{-2}))^{-0.5}$. If we substitute $\Sigma_{\text{H}_2} = f_{\text{H}_2, \text{GMC}}(\Sigma_{\text{gas}}) \approx 200 \text{ M}_{\odot} \text{ pc}^{-2}$ and $Z = 0.5 Z_{\odot}$ we obtain $\alpha_{\text{CO}} = 2.9 \text{ M}_{\odot}/(\text{K km s}^{-1} \text{ pc}^2)$ in agreement within a factor ≈ 2 with our results.

4.5 ALMA observability

In Section 4.3 we have shown that the peak of the Althaea CO SLED coincides with the CO(7–6) line. As CO transitions with $J_{\text{up}} \geq 6$ fall in the ALMA bands from $z > 6$, in what follows, we use the ALMA Sensitivity Calculator to compute the observing time required to detect the CO(7–6) line from (a galaxy similar to) Althaea. The total CO(7–6) luminosity of Althaea is $L_{\text{CO}(7-6)} = 10^{7.1} L_{\odot}$, i.e. $\approx 1/16$ of its [C II] luminosity. If we assume the line width to be equal to that of [C II] observations in LBGs at $z \approx 6 - 7$ (FWHM $\approx 150 \text{ km s}^{-1}$ Maiolino et al. 2015; Knudsen et al. 2016; Pentericci et al. 2016; Bradač et al. 2017), this yields a peak flux density $F_{\text{CO}(7-6)}^p \approx 0.179 \text{ mJy}$.⁸ The ALMA full-array observing time required to detect (resolve over $1/3 \times \text{FWHM}$) the CO(7–6) line with a signal-to-noise ratio $S/N = 5$ is $\approx 13 \text{ h}$ ($\approx 38 \text{ h}$), i.e. it would be challenging but doable within the maximum observing time ($\leq 50 \text{ h}$) allowed for ALMA regular programs. This is in line with what was found by Muñoz & Furlanetto (2013), which pointed out that ALMA observations of high- J CO can be performed with reasonable integration times only in those $z \approx 6$ galaxies which, like Althaea, are chemically evolved ($Z_{\text{Althaea}} > 0.1 Z_{\odot}$) and UV-bright ($M_{\text{UV, Althaea}} \approx -22$).

5 CONCLUSIONS

In this paper we have studied the CO emission properties of galaxies at the end of the Reionization Epoch. First, we have developed a semi-analytical model that, given the internal density field of a GMC and the impinging FUV flux (G_0) at the cloud surface, computes the CO line emission. The density PDF of the GMC is set both by turbulence (parametrized by the Mach number \mathcal{M}) and self-gravity (parametrized by t/t_{ff}). The radiative transfer is performed with CLOUDY and includes $z = 6$ CMB radiation. The model takes

⁸ The peak flux is related to the luminosity in solar units by the following equation (Obreschkow et al. 2009):

$$\frac{F_{\text{CO}}^p}{\text{Jy}} = 961.5 \frac{L_{\text{CO}}}{L_{\odot}} \left(\frac{D_L}{\text{Mpc}} \right)^{-2} \left(\frac{\nu_o}{\text{GHz}} \right)^{-1} \left(\frac{\text{FWHM}}{\text{km s}^{-1}} \right)^{-1},$$

where D_L is the luminosity distance to the source in Mpc, and ν_o is the observed frequency in GHz.

the mean gas density n_0 , \mathcal{M} , t/t_{ff} , G_0 as inputs, and it returns the luminosity of the first nine CO rotational transitions. We validated the model with local observations, demonstrating its capability to reproduce:

- (i) the $M_{\text{vir}}-L'_{\text{CO}}$ relation;
- (ii) the observed CO excitation in local SB galaxies; and
- (iii) the CO SLED of the low-metallicity ($Z \approx 0.5 Z_{\odot}$) molecular cloud N159W in the LMC.

We used our validated CO emission model to post-process a cosmological zoom-in simulation of a prototypical $z \approx 6$ galaxy ($M_{\star} \sim 10^{10} M_{\odot}$, $\text{SFR} \sim 100 M_{\odot} \text{yr}^{-1}$), Althæa. We have made the following additional assumptions: (i) we adopt a constant CRIR (cfr. Appendix B for a discussion on the effects of the CRIR variation); (ii) the dust-to-gas ratio scales linearly with metallicity; (iii) all clumps within a GMCs are exposed to the same (external) FUV flux predicted by the simulation; and (iv) photoevaporation of clumps affecting the density field and the lifetime of GMCs has been neglected.

The key results can be summarized as follows:

1. The CO emission traces the innermost disc of Althæa where most of the H_2 mass resides.
2. The CO(1–0) luminosity of Althæa is comparable to that of the MS galaxies with similar stellar mass at $z \approx 0$. As the MS evolves with redshift, and the sSFR increases, this means that the CO(1–0) per unit SFR in Althæa is lower than measured in local galaxies.
3. The CO-to- H_2 conversion factor is $\langle \alpha_{\text{CO}} \rangle = 1.54 \pm 0.9 M_{\odot} / (\text{K km s}^{-1} \text{pc}^2)$ with little spatial variation throughout the disc. The dispersion is primarily introduced by density variations in the Althæa disc.
4. The maximum of the CO(1–0) and CO(7–6) surface brightnesses are co-located in the disc ($S_{\text{CO}(1-0)} \approx 10^5 L_{\odot} \text{kpc}^{-2}$ and $S_{\text{CO}(7-6)} \approx 10^{7.2} L_{\odot} \text{kpc}^{-2}$, respectively).
5. The suppression of the observed CO luminosity due to the CMB at high- z is compensated by the increased temperature of GMCs. The net result is both an increase of the CO SLED excitation and a shift of the peak at higher J .
6. The peak of the Althæa CO SLED coincides with the CO(7–6) transition and $L_{\text{CO}(7-6)} = 10^{7.1} L_{\odot}$ i.e. $\approx 1/16$ of the [CII] luminosity. This is due to the relatively high surface density of Althæa and to the warm temperature ($T_{\text{k}} \approx 45 \text{ K}$) of the GMCs. To resolve the CO(7–6) line with a S/N = 5 an ALMA observing time of $\approx 38 \text{ h}$ is required.

ACKNOWLEDGEMENTS

We thank G. Ucci, D. Cormier, R. Maiolino, M. Bothwell for useful discussions. We thank the anonymous referee for the valuable feedback that increased the clarity of the paper. AF acknowledges support from the ERC Advanced Grant INTERSTELLAR H2020/740120. ES acknowledges support from the Israeli Science Foundation under Grant No. 719/14.

REFERENCES

- Abel N. P., Ferland G. J., Shaw G., van Hoof P. A. M., 2005, *ApJS*, 161, 65
- Agertz O., Kravtsov A. V., 2015, *ApJ*, 804, 18
- Aravena M. et al., 2016, *MNRAS*, 457, 4406
- Baker A., Tacconi L., Genzel R., Lehnert M., Lutz D., 2004, in Aalto S., Hüttemeister S., Pedlar A., eds, *ASP Conf. Ser. Vol. 320, The Neutral ISM in Starburst Galaxies*. Astron. Soc. Pac., San Francisco, p. 338
- Bertoldi F. et al., 2003, *A&A*, 409, L47
- Bisbas T. G., Papadopoulos P. P., Viti S., 2015, *ApJ*, 803, 37
- Bolatto A. D., Leroy A. K., Rosolowsky E., Walter F., Blitz L., 2008, *ApJ*, 686, 948
- Bolatto A. D., Wolfire M., Leroy A. K., 2013, *ARA&A*, 51, 207
- Bradač M. et al., 2017, *ApJ*, 836, L2
- Bradford C. M., Nikola T., Stacey G. J., Bolatto A. D., Jackson J. M., Savage M. L., Davidson J. A., Higdon S. J., 2003, *ApJ*, 586, 891
- Carilli C. L., Walter F., 2013, *ARA&A*, 51, 105
- Cazaux S., Tielens A. G. G. M., 2004, *ApJ*, 604, 222
- Chevance M. et al., 2016, *A&A*, 590, A36
- Cicone C. et al., 2017, *A&A*, 604, A53
- Clark P. C., Glover S. C. O., 2015, *MNRAS*, 452, 2057
- Combes F. et al., 2012, *A&A*, 538, L4
- Coppin K. E. K. et al., 2007, *ApJ*, 665, 936
- Cowie L. L., Songaila A., 1986, *ARA&A*, 24, 499
- da Cunha E. et al., 2013, *ApJ*, 766, 13
- Dayal P., Ferrara A., Gallerani S., 2008, *MNRAS*, 389, 1683
- Dayal P., Ferrara A., Saro A., Salvaterra R., Borgani S., Tornatore L., 2009, *MNRAS*, 400, 2000
- De Looze I. et al., 2014, *A&A*, 568, A62
- Decarli R. et al., 2016, *ApJ*, 833, 69
- Decataldo D., Ferrara A., Pallottini A., Gallerani S., Vallini L., 2017, *MNRAS*, 471, 4476
- Dessauges-Zavadsky M. et al., 2015, *A&A*, 577, A50
- Dessauges-Zavadsky M. et al., 2016, *A&A*, 605, A81
- Federrath C., Klessen R. S., 2013, *ApJ*, 763, 51
- Ferland G. J., Fabian A. C., Johnstone R. M., 1994, *MNRAS*, 266, 399
- Ferland G. J. et al., 2013, *Rev. Mex. Astron. Astrofis.*, 49, 137
- Fukui Y. et al., 2015, *ApJ*, 807, L4
- Gallerani S., Ferrara A., Neri R., Maiolino R., 2014, *MNRAS*, 445, 2848
- Gallerani S., Fan X., Maiolino R., Pacucci F., 2017, *PASA*, 34, e022
- Ginolfi M. et al., 2017, *MNRAS*, 468, 3468
- Girichidis P., Konstantin L., Whitworth A. P., Klessen R. S., 2014, *ApJ*, 781, 91
- Glassgold A. E., Langer W. D., 1974, *ApJ*, 193, 73
- Glover S. C. O., Clark P. C., 2012, *MNRAS*, 421, 9
- Glover S. C. O., Clark P. C., 2016, *MNRAS*, 456, 3596
- Glover S. C. O., Mac Low M.-M., 2011, *MNRAS*, 412, 337
- Glover S. C. O., Federrath C., Mac Low M.-M., Klessen R. S., 2010, *MNRAS*, 404, 2
- Goldsmith P. F., Heyer M., Narayanan G., Snell R., Li D., Brunt C., 2008, *ApJ*, 680, 428
- Goodman A. A., Pineda J. E., Schnee S. L., 2009, *ApJ*, 692, 91
- Gorti U., Hollenbach D., 2002, *ApJ*, 573, 215
- Grassi T., Bovino S., Schleicher D. R. G., Prieto J., Seifried D., Simoncini E., Gianturco F. A., 2014, *MNRAS*, 439, 2386
- Habing H. J., 1968, *Bull. Astron. Inst. Netherlands*, 19, 421
- Hennebelle P., Chabrier G., 2011, *ApJ*, 743, L29
- Hennebelle P., Chabrier G., 2013, *ApJ*, 770, 150
- Hollenbach D. J., Tielens A. G. G. M., 1999, *Rev. Mod. Phys.*, 71, 173
- Indriolo N., Geballe T. R., Oka T., McCall B. J., 2007, *ApJ*, 671, 1736
- Indriolo N., Bergin E. A., Goicoechea J. R., Cernicharo J., Gerin M., Gusdorf A., Lis D. C., Schilke P., 2017, *ApJ*, 836, 117
- Jiang L. et al., 2016, *ApJ*, 816, 16
- Jura M., 1975, *ApJ*, 197, 575
- Kainulainen J., Lada C. J., Rathborne J. M., Alves J. F., 2009, *A&A*, 497, 399
- Kaufman M. J., Wolfire M. G., Hollenbach D. J., Luhman M. L., 1999, *ApJ*, 527, 795
- Kazandjian M. V., Pelupessy I., Meijerink R., Israel F. P., Coppola C. M., Rosenberg M. J. F., Spaans M., 2016, *A&A*, 595, A124
- Kim W.-T., Ostriker E. C., Stone J. M., 2003, *ApJ*, 599, 1157
- Knudsen K. K., Richard J., Kneib J.-P., Jauzac M., Clément B., Drouart G., Egami E., Lindroos L., 2016, *MNRAS*, 462, L6
- Krumholz M. R., McKee C. F., 2005, *ApJ*, 630, 250
- Krumholz M. R., McKee C. F., Tumlinson J., 2009, *ApJ*, 693, 216
- Krumholz M. R., Dekel A., McKee C. F., 2012, *ApJ*, 745, 69

- Lagos C. d. P., Bayet E., Baugh C. M., Lacey C. G., Bell T. A., Fanidakis N., Geach J. E., 2012, *MNRAS*, 426, 2142
- Larson R. B., 1981, *MNRAS*, 194, 809
- Le Teuff Y. H., Millar T. J., Markwick A. J., 2000, *A&AS*, 146, 157
- Lee M.-Y. et al., 2016, *A&A*, 596, A85
- Leitherer C. et al., 1999, *APJS*, 123, 3
- Lejeune T., Cuisinier F., Buser R., 1997, *A&AS*, 125
- Leroy A. K. et al., 2011, *ApJ*, 737, 12
- Liszt H. S., 2007, *A&A*, 461, 205
- Livermore R. C. et al., 2012, *ApJ*, 758, L35
- Lombardi M., Alves J., Lada C. J., 2015, *A&A*, 576, L1
- Lu N. et al., 2017, *ApJS*, 230, 1
- Magdis G. E. et al., 2011, *ApJ*, 740, L15
- Maiolino R. et al., 2007, *A&A*, 472, L33
- Maiolino R. et al., 2015, *MNRAS*, 452, 54
- Mashian N. et al., 2015, *ApJ*, 802, 81
- McKee C. F., Ostriker E. C., 2007, *ARA&A*, 45, 565
- Meijerink R., Spaans M., Israel F. P., 2007, *A&A*, 461, 793
- Molina F. Z., Glover S. C. O., Federrath C., Klessen R. S., 2012, *MNRAS*, 423, 2680
- Muñoz J. A., Furlanetto S. R., 2013, *MNRAS*, 435, 2676
- Narayanan D., Krumholz M. R., 2014, *MNRAS*, 442, 1411
- Narayanan D., Krumholz M., Ostriker E. C., Hernquist L., 2011, *MNRAS*, 418, 664
- Narayanan D., Krumholz M. R., Ostriker E. C., Hernquist L., 2012, *MNRAS*, 421, 3127
- Obreschkow D., Heywood I., Klöckner H.-R., Rawlings S., 2009, *ApJ*, 702, 1321
- Ostriker E. C., Stone J. M., Gammie C. F., 2001, *ApJ*, 546, 980
- Padoan P., Nordlund Å., 2011, *ApJ*, 730, 40
- Padovani M., Galli D., Glassgold A. E., 2009, *A&A*, 501, 619
- Pallottini A., Ferrara A., Gallerani S., Salvadori S., D’Odorico V., 2014, *MNRAS*, 440, 2498
- Pallottini A., Gallerani S., Ferrara A., Yue B., Vallini L., Maiolino R., Feruglio C., 2015, *MNRAS*, 453, 1898
- Pallottini A., Ferrara A., Bovino S., Vallini L., Gallerani S., Maiolino R., Salvadori S., 2017a, *MNRAS*, 471, 4128
- Pallottini A., Ferrara A., Gallerani S., Vallini L., Maiolino R., Salvadori S., 2017b, *MNRAS*, 465, 2540
- Papadopoulos P. P., van der Werf P. P., Xilouris E. M., Isaak K. G., Gao Y., Mühle S., 2012, *MNRAS*, 426, 2601
- Pentericci L. et al., 2016, *ApJ*, 829, L11
- Pineda J. E., Caselli P., Goodman A. A., 2008, *ApJ*, 679, 481
- Pineda J. L., Ott J., Klein U., Wong T., Muller E., Hughes A., 2009, *ApJ*, 703, 736
- Pon A., Johnstone D., Kaufman M. J., 2012, *ApJ*, 748, 25
- Pon A., Caselli P., Johnstone D., Kaufman M., Butler M. J., Fontani F., Jiménez-Serra I., Tan J. C., 2015, *A&A*, 577, A75
- Pon A. et al., 2016, *ApJ*, 827, 107
- Popping G., van Kampen E., Decarli R., Spaans M., Somerville R. S., Trager S. C., 2016, *MNRAS*, 461, 93
- Pozzi F., Vallini L., Vignali C., Talia M., Gruppioni C., Mingozzi M., Massardi M., Andreani P., 2017, *MNRAS*, 470, L64
- Rebolledo D., Wong T., Xue R., Leroy A., Koda J., Donovan Meyer J., 2015, *ApJ*, 808, 99
- Renzini A., Peng Y.-j., 2015, *ApJ*, 801, L29
- Riechers D. A. et al., 2010a, *ApJ*, 720, L131
- Riechers D. A., Carilli C. L., Walter F., Momjian E., 2010b, *ApJ*, 724, L153
- Rolleston W. R. J., Trundle C., Dufton P. L., 2002, *A&A*, 396, 53
- Rosenberg M. J. F. et al., 2015, *ApJ*, 801, 72
- Saintonge A. et al., 2011, *MNRAS*, 415, 32
- Saintonge A. et al., 2013, *ApJ*, 778, 2
- Sandstrom K. M. et al., 2013, *ApJ*, 777, 5
- Savage B. D., Sembach K. R., 1996, *ApJ*, 470, 893
- Schaefer B. E., 2008, *AJ*, 135, 112
- Schaefer D., Boone F., Zamojski M., Staguhn J., Dessauges-Zavadsky M., Finkelstein S., Combes F., 2015, *A&A*, 574, A19
- Schaller G., Schaefer D., Meynet G., Maeder A., 1992, *A&AS*, 96, 269
- Schmutz W., Leitherer C., Gruenwald R., 1992, *PASP*, 104, 1164
- Schneider N. et al., 2016, *A&A*, 587, A74
- Shaw G., Ferland G. J., Abel N. P., Stancil P. C., van Hoof P. A. M., 2005, *ApJ*, 624, 794
- Shetty R., Glover S. C., Dullemond C. P., Klessen R. S., 2011, *MNRAS*, 412, 1686
- Solomon P. M., Vanden Bout P. A., 2005, *ARA&A*, 43, 677
- Solomon P. M., Rivolo A. R., Barrett J., Yahil A., 1987, *ApJ*, 319, 730
- Speagle J. S., Steinhardt C. L., Capak P. L., Silverman J. D., 2014, *ApJS*, 214, 15
- Stutz A. M., Kainulainen J., 2015, *A&A*, 577, L6
- Tacconi L. J. et al., 2008, *ApJ*, 680, 246
- Tasker E. J., Tan J. C., 2009, *ApJ*, 700, 358
- Teyssier R., 2002, *A&A*, 385, 337
- Vallini L., Dayal P., Ferrara A., 2012, *MNRAS*, 421, 3266
- Vallini L., Gallerani S., Ferrara A., Baek S., 2013, *MNRAS*, 433, 1567
- Vallini L., Gallerani S., Ferrara A., Pallottini A., Yue B., 2015, *ApJ*, 813, 36
- Vallini L., Gruppioni C., Pozzi F., Vignali C., Zamorani G., 2016, *MNRAS*, 456, L40
- Vallini L., Ferrara A., Pallottini A., Gallerani S., 2017, *MNRAS*
- Vazquez-Semadeni E., 1994, *ApJ*, 423, 681
- Venemans B. P. et al., 2012, *ApJ*, 751, L25
- Wada K., 2008, *ApJ*, 675, 188
- Wagg J., Kanekar N., 2012, *ApJ*, 751, L24
- Wagg J., Kanekar N., Carilli C. L., 2009, *ApJ*, 697, L33
- Walter F. et al., 2012, *ApJ*, 752, 93
- Walter F. et al., 2014, *ApJ*, 782, 79
- Wang R. et al., 2010, *ApJ*, 714, 699
- Weingartner J. C., Draine B. T., 2001, *ApJ*, 548, 296
- Weiß A., Downes D., Neri R., Walter F., Henkel C., Wilner D. J., Wagg J., Wiklind T., 2007, *A&A*, 467, 955
- Weiß A. et al., 2013, *ApJ*, 767, 88
- Wolfire M. G., Hollenbach D., McKee C. F., 2010, *ApJ*, 716, 1191
- Wong T. et al., 2011, *ApJS*, 197, 16
- Yao L., Seaquist E. R., Kuno N., Dunne L., 2003, *ApJ*, 588, 771

APPENDIX A: TIME EVOLUTION OF THE DENSITY PDF OF A GMC

Following Girichidis et al. (2014), we first consider a homogeneous sphere, with initial density ρ_0 , collapsing under its own gravity. The density at any later time t can be well approximated by

$$\rho = \rho_0 \left[1 - \left(\frac{t}{t_{\text{ff}}} \right)^2 \right]^{-2}, \quad (\text{A1})$$

where

$$t_{\text{ff}} \equiv \sqrt{\frac{3\pi}{32G\rho_0}} \quad (\text{A2})$$

is the free-fall time of the sphere.

Due to the conservation of the probability density, one can calculate the evolved density PDF as

$$P_V(\rho, t) = P_V(\rho_0, 0) \frac{d\rho_0}{d\rho}, \quad (\text{A3})$$

where ρ_0 needs to be expressed as a function of ρ and t inverting equation (A1).

APPENDIX B: EFFECT OF VARYING THE COSMIC RAY IONIZATION RATE

In our simulations we assume $\zeta_{\text{CR}} = 2 \times 10^{-16} \text{ s}^{-1}$ (Indriolo et al. 2007). This value is $\approx 20\times$ higher than the CRIR ($\zeta_{\text{CR},0} = 10^{-17} \text{ s}^{-1}$) generally adopted as default in many PDR calculations

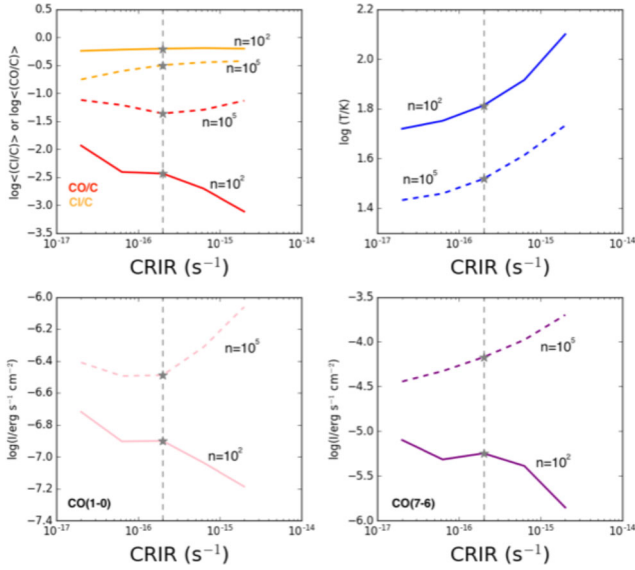


Figure B1. Upper left panel: variation of the average $\langle n_{\text{CO}}/n_{\text{C}} \rangle$ and $\langle n_{\text{CI}}/n_{\text{C}} \rangle$ ratios for $n = 10^2 \text{ cm}^{-3}$ (solid lines) and $n = 10^5 \text{ cm}^{-3}$ (dashed lines) as a function of the CRIR. Upper right: variation of the gas temperature at $N_{\text{H}} = 10^{22} \text{ cm}^{-2}$. Bottom left: variation of the CO(1–0) emissivity. Bottom right: variation of the CO(7–6) emissivity. The dashed vertical line highlights the CRIR adopted in this work.

(e.g. Glover & Clark 2012; Bisbas, Papadopoulos & Viti 2015). The actual CRIR value in Althæa – and in general in high- z galaxies – is highly uncertain, owing to e.g. the unknown magnetic field in the ISM of high- z galaxies.

A simple estimate of the CRIR can be obtained assuming a linear scaling with the SFR, as the main source of CRs is the Fermi acceleration in supernova (SNe) remnants, and the rate of SNe is related to the rate at which stars form. In Althæa the $\text{SFR} \approx 100 M_{\odot} \text{ yr}^{-1}$, thus, a linear CRIR–SFR scaling would imply $\zeta_{\text{CR, Althæa}} \approx \zeta_{\text{CR,0}} \times \text{SFR} \approx 10^{-15} \text{ s}^{-1}$ i.e. at most a factor of 5 greater than the value adopted in our CLOUDY simulations.

To test the impact of the CRIR variation on the CO (and CI) abundance, gas temperature and CO line emissivity, we run a set of CLOUDY models with CRIR in the range $[2 \times 10^{-17} - 2 \times 10^{-15}] \text{ s}^{-1}$, keeping $G_0 = 100$ and $Z = 0.5 Z_{\odot}$ fixed to the fiducial values of Althæa. In Fig. B1, we show the variation of the $\langle n_{\text{CO}}/n_{\text{C}} \rangle$ and $\langle n_{\text{CI}}/n_{\text{C}} \rangle$ ratios (upper left panel), gas temperature (upper right) at $N_{\text{H}} = 10^{22} \text{ cm}^{-2}$, CO(1–0) emissivity (bottom left), CO(7–6) emissivity (bottom right) that we obtain in two different set of CLOUDY runs at fixed gas number density $n = 10^2 \text{ cm}^{-3}$ and $n = 10^5 \text{ cm}^{-3}$. The $\langle n_{\text{CO}}/n_{\text{C}} \rangle$ and $\langle n_{\text{CI}}/n_{\text{C}} \rangle$ ratios are obtained by averaging the $\langle n_{\text{CO}}(r)/n_{\text{C}} \rangle$ and $\langle n_{\text{CI}}(r)/n_{\text{C}} \rangle$ returned by CLOUDY as a function of the depth (r) into the gas slab. These values are proportional to the total fraction of carbon locked up in CO and CI, respectively.

We note that at low densities ($n = 10^2 \text{ cm}^{-3}$, solid lines) $\langle n_{\text{CO}}/n_{\text{C}} \rangle$ decreases with increasing CRIR, while the opposite is true for $\langle n_{\text{CI}}/n_{\text{C}} \rangle$. This trend is expected as an increase of CRIR produces more He^+ . This ultimately boosts the dissociative charge transfer reactions of the CO molecules with He^+ ions. In shielded regions the ionized carbon produced by these reactions is then converted into neutral carbon boosting the CI/C ratio. Note, however, that a 100x variation in the CRIR causes a drop of $\approx 1/10$ in $\langle n_{\text{CO}}/n_{\text{C}} \rangle$. As expected, the gas temperature, sampled at $N_{\text{H}} = 10^{22} \text{ cm}^{-2}$, increases

with CRIR, as the heating provided by CRs is proportional to the cosmic rate ionization rate. The CO(1–0) and the CO(7–6) emissivities decrease of ≈ 0.6 dex, as the boost in the gas temperature is not enough to compensate for the CO abundance decrease.

At high densities ($n = 10^5 \text{ cm}^{-3}$, dashed lines) the situation is slightly different. The $\langle n_{\text{CO}}/n_{\text{C}} \rangle$ ratio decreases only of a factor ≈ 2 between CRIR $[2 \times 10^{-17} - 2 \times 10^{-16}] \text{ s}^{-1}$ and $\langle n_{\text{CO}}/n_{\text{C}} \rangle$ remains almost constant, with a very shallow increase above $\zeta_{\text{CR}} = 1 \times 10^{-15} \text{ s}^{-1}$. The higher temperature makes the CO(1–0) and CO(7–6) emissivity increase of $\approx 0.4 - 0.5$ dex, respectively, for CRIR varying between $[2 \times 10^{-17} - 2 \times 10^{-15}] \text{ s}^{-1}$, and compensate the small CO drop. This is in line with Bisbas et al. (2015, see their fig. 3) and Glover & Clark (2016), who note that very dense clumps remain CO-bright despite the increase of the cosmic rate ionization rate.

As pointed out by Glover & Clark (2016), accounting for the influence of turbulence on the density field of GMCs when assessing the impact of the CRIR variation on the CO emission is pivotal, as a significant GMC mass fraction may be located in regions with a mean density higher than the volume-weighted mean density of the cloud. Glover & Clark (2016) show that, in this case, a variation of CRIR by a factor of 100 has only a minor effect on e.g. the values of the α_{CO} conversion factor. Given that, and the results shown in Fig. B1, we expect that uncertainties on the CRIR of a factor of 5 cause a negligible variation in the CO line luminosity. This is especially true for the CO(7–6) line (owing to the high critical density of the transition, $n_{\text{cr}} = 4.5 \times 10^5 \text{ cm}^{-3}$) for which we provide our ALMA predictions.

APPENDIX C: MOLECULAR FRACTION FROM THE SUB-GRID MODEL

As we are interested in how efficiently the CO luminosity traces the H_2 mass and given that L_{CO} is computed through the sub-grid model, we need the actual molecular mass returned by the model itself. The molecular fraction from the hydrodynamical simulation ($f_{\text{H}_2, \text{sim}}$) – that does not account for the internal density structure of the GMCs – underestimates the molecular mass as $f_{\text{H}_2, \text{sim}} < f_{\text{H}_2, \text{GMC}}$ and hence predicts an artificially low conversion factor.

The molecular fraction from the sub-grid model ($f_{\text{H}_2, \text{GMC}}$) has been calculated through the following procedure. Let $f_{\text{H}_2}(\rho_i, r)$ be the H_2/HI radial profile returned by CLOUDY for the gas slab of constant density $n_i = \rho_i/m_p$, illuminated by FUV flux G_0 at the surface, and characterized by a gas metallicity Z . We remind the reader that the radius, r_i , column density, N_i , of the various clumps are set by equation (5). The H_2 mass of each clump of constant density n_i is

$$m_{\text{H}_2}^i = 2m_p n_i \int_0^{r_i} 4\pi f_{\text{H}_2}(n_i, r) r^2 dr. \quad (\text{C1})$$

The molecular fraction of each GMC is then

$$f_{\text{H}_2, \text{GMC}} = \frac{M_{\text{H}_2, \text{tot}}}{M_{\text{GMC}}} = \frac{\sum_i m_{\text{H}_2, i}}{\sum_i m_{\text{tot}}^i} \quad (\text{C2})$$

In Fig. C1 we plot $f_{\text{H}_2, \text{GMC}}$ as a function of the mean density n_0 and Mach number \mathcal{M} assuming G_0 and Z equal to those of Althæa. We note that the molecular fraction increases with n_0 and \mathcal{M} . For values $n_0 = \langle n_0 \rangle = 10^{2.5} \text{ cm}^{-3}$ and $\mathcal{M} = 30$, i.e. those typical of Althæa molecular disc, we obtain $f_{\text{H}_2, \text{GMC}} \approx 0.9$.

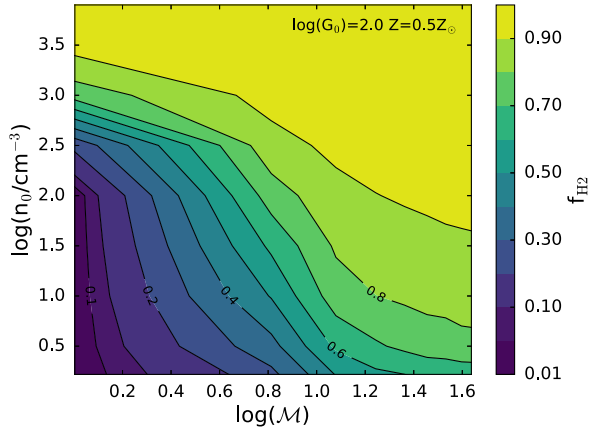


Figure C1. Molecular fraction as a function of n_0 and \mathcal{M} . We fix G_0 and Z to those of Althæa.

This paper has been typeset from a \LaTeX file prepared by the author.